

MOLECULAR BEAM EPITAXY GROWTH AND CHARACTERIZATION OF
GERMANIUM TIN CARBIDE MULTIPLE QUANTUM WELL
STRUCTURES

by

Augustus Wolf Arbogast, B.S. Physics

A thesis submitted to the Graduate Council of
Texas State University in partial fulfillment
of the requirements for the degree of
Master of Science
with a Major in Materials Physics
December 2022

Committee Members:

Mark Wistey, Chair

Mark Holtz

Edwin Piner

COPYRIGHT

by

Augustus Wolf Arbogast

2022

FAIR USE AND AUTHOR'S PERMISSION STATEMENT

Fair Use

This work is protected by the Copyright Laws of the United States (Public Law 94-553, section 107). Consistent with fair use as defined in the Copyright Laws, brief quotations from this material are allowed with proper acknowledgement. Use of this material for financial gain without the author's express written permission is not allowed.

Duplication Permission

As the copyright holder of this work I, Augustus Wolf Arbogast, authorize duplication of this work, in whole or in part, for educational or scholarly purposes only.

DEDICATION

I'd like to dedicate this work to the friends I made along the way, and to my father for always being there with a smile.

ACKNOWLEDGEMENTS

This work was made possible only with the help of some truly stellar people in my life. I would not be where I am today without their help.

First and foremost, I'd like to acknowledge my advisor, Dr. Mark Wistey, as the officiate and premier aid and mentor in my time here. Many of my past triumphs and failures were celebrated with him, and it's from these experiences I was able to muster the will power and know-how in the completion of this thesis.

Secondly, I'd like to mention two special fellow researchers/friends: Dr. Shamim Reza and Mr. (soon-to-be-Dr.) Tuhin Dey. I've spent countless hours in the presence of these two gentlemen, be they in the lab, the coffee shop, on an airplane, or dinner at one of our places. I especially thank them for the gift that learning in groups grants us all, and for their delicious cooking.

Next, my committee members: Thanks to Dr. Mark Holtz for being there as often and as welcoming as you were, particularly in my mad dash to the finish line. Also, thanks to Dr. Edwin Piner for the discussions we've had over the years.

Thanks to the physics department writ-large for the support over the years (and to William and Christie in the front office!). Much of my formative time as an undergrad at Texas State was found mostly in the halls of the third floor of RFM, often working late hours into the night to solve homework problems with friends. I wish to impart a particular thanks to Drs. Hunter and Eleanor Close, Dr. David Donnelly, Dr. Wilhelmus Geerts, Dr. Brandon Lunk, Dr. Blagoy Rangelov, and Dr. Nikoleta Theodoropoulou.

Naturally, I couldn't have done it without the help of my physics friends/colleagues along the way. There are too many to mention here.

Thanks to Dr. Casey Smith and Dr. Alissa Savage and the ARSC for access to the tools necessary to finish the work in this thesis (and for putting up with my learning them!).

Finally, thanks to my parents for believing in me and granting me the opportunity to be here in the first place!

TABLE OF CONTENTS

	Page
ACKNOWLEDGEMENTS	v
LIST OF FIGURES	ix
LIST OF ABBREVIATIONS.....	xi
CHAPTER	
1. INTRODUCTION	1
1.1: Motivation.....	1
1.2: Route to Direct Bandgap Germanium	2
1.3: GeSnC Quantum Wells.....	6
1.4: Growth and Characterization: Bulk and MQW Heterostructures.....	7
1.5: Summary	7
2. BULK EPITAXIAL THIN FILM GROWTH AND CHARACTERIZATION ..	9
2.1: Molecular Beam Epitaxy	9
2.2: Bulk Germanium.....	12
2.3: P-Type Doping, Ge:Ga	14
2.4: Bulk $\text{Ge}_{1-x}\text{C}_x$ and $\text{Ge}_{1-y}\text{Sn}_y$	16
2.4.1: Gas Precursors: Carbon Tetrabromide and Hydrogen	16
2.4.2: $\text{Ge}_{1-x}\text{C}_x$	18
2.4.3: $\text{Ge}_{1-y}\text{Sn}_y$	20
2.5: $\text{Ge}_{1-x-y}\text{Sn}_x\text{C}_y$	20
3. MULTIPLE QUANTUM WELL EPITAXIAL THIN FILM GROWTH AND CHARACTERIZATION	23
3.1: First MQW Growth: GeSnC/Ge on Semi-insulating GaAs Substrate	23
3.2: Characterization	25
3.2.1: RHEED	25
3.2.2: X-Ray Diffraction	26
3.2.3: Photoluminescence	28
4. TOWARD BETTER-QUALITY MATERIAL	31

4.1: Changes and Improvements.....	31
4.1.1: System Improvement and Additions.....	31
4.1.2: MQW Changes and Improvement	32
4.1.3: Material Characterization Improvement.....	33
4.2: Other Characterization Techniques	34
4.2.1: Atomic Force Microscopy	34
4.2.2: Absorption	36
4.3: Growths and Discussion	38
4.3.1: GeSnC/Ge on Semi-insulating GaAs Substrate.....	38
4.3.2: GeSnC/Ge on P-Type Ge Substrate.....	40
4.3.3: Direct Absorption of Bulk GeSnC.....	43
 5. CONCLUSION AND FUTURE WORKS	 46
5.1: Conclusion and Impact	46
5.2: Summary	47
5.3: Future Work.....	48
5.3.1: Optimizing GeSnC MQW Heterostructures	48
5.3.2: Device Fabrication.....	49
 APPENDIX.....	 50
 REFERENCE/LITERATURE CITED	 61

LIST OF FIGURES

Figure	Page
1.1: Moore’s Law trendline.....	1
1.2: (a) Schematic band structure of bulk Ge, (b) schematic band structure of bulk Ge under tensile strain, (c) electron injection of Ge under tensile strain	3
1.3: Sketches of the band diagrams for (a) germanium and (b) gallium arsenide	4
1.4: Band diagram of GeSnC heterostructure	6
2.1: Varian Gen-II MBE system	10
2.2: Wistey Group Varian Gen-II Group-IV MBE system.....	11
2.3: Wistey Group Veeco Gen 930 III-V MBE system.....	12
2.4: Texas State SRO Bio-RAD Hall measurement system	15
2.5: Carbon tetrabromide molecule.....	17
2.6: Tetragermymethane (4GeMe) molecule.....	18
2.7: (a)-(c) RHEED images of samples grown under atomic-H at 215 °C, 270 °C, and 324 °C, respectively	19
2.8: (a)-(c) 5×5 μm ² AFM images of samples grown under atomic-H at 215 °C, 270 °C, and 324 °C, respectively	20
2.9: (a)-(c) 2×2 μm ² AFM images of GeSn samples grown at 160 °C, 180 °C, and 200 °C, respectively	20
2.10: (a) Ge _{1-x-y} Sn _x C _y HR-XRD 2Theta-Omega scans about (004), (b) RSM around (115) plane for the 160 °C sample	21
2.11: (a)-(e) RHEED for Ge _{1-x-y} Sn _x C _y growths at various temperatures	22
3.1: First GeSnC/Ge MQW heterostructure, grown on semi-insulating GaAs.....	23

3.2: RHEED Diagram	25
3.3: Bragg's Law diagram.....	26
3.4: Texas State SRO Rigaku XRD system	27
3.5: 2θ - ω XRD scan of first GeSnC/Ge MQW on GaAs substrate (red), GlobalFit simulation peak-fit (blue).....	28
3.6: Photoluminescence of first MQW sample	30
4.1: Bruker Dimension ICON AFM, Texas State University SRO	35
4.2: Two newest MQW growths on semi-insulating GaAs after improved growth techniques	38
4.3: AFM measurement of GeSnC MQW on semi-insulating GaAs after process upgrades (left), AFM measurement of atomic-hydrogen-treated GaAs growth surface after 2-hour 350 °C bake showing no segregation.....	39
4.4: XRD measurement of GeSnC MQW on semi-insulating GaAs after improvements in growth technique.....	40
4.5: (left) RHEED surface reconstruction of first QW layer of GeSnC on p-Ge, (right) p- Ge growth surface after atomic-H and 700 °C desorption treatment.....	41
4.6: AFM measurement of GeSnC MQW structure on p-Ge sample grown at 160 °C	42
4.7: PL measurement of GeSnC MQW structure on p-Ge sample grown at 160 °C.....	42
4.8: PL measurements of three different MQW samples on a linear scale.....	43
4.9: Direct bandgap absorption plot of bulk GeSnC.....	44
A1.1: Microscope slide with slide cover over anemic goat blood sample.....	60

LIST OF ABBREVIATIONS

Abbreviation	Description
AFM	Atomic Force Microscopy
ARSC	Analysis Research Service Center
BEP	Beam-Equivalent Pressure
CAR	Continual Azimuthal Rotation
CMOS	Complementary Metal Oxide Semiconductor
CVD	Chemical Vapor Deposition
FWHM	Full Width Half Maxima
Ge	Germanium
GeC	Germanium Carbon
GeSn	Germanium Tin
GeSnC	Germanium Tin Carbon
HH	Heavy Hole
HRXRD	High-Resolution X-Ray Diffraction
LH	Light Hole
MBE	Molecular Beam Epitaxy
MFC	Mass Flow Controller
MQW	Multiple Quantum Well

MSEC	Materials Science, Engineering, and Commercialization
NRSC	Nano Research Service Center
NSF	National Science Foundation
PL	Photoluminescence
QW	Quantum Well
RBS	Rutherford Backscattering Spectroscopy
RGA	Residual Gas Analyzer
RHEED	Reflection High-Energy Electron Diffraction
RMS	Root Mean Square
RPM	Rotations Per Minute
RSM	Reciprocal Space Mapping
SEM	Scanning Electron Microscopy
Si	Silicon
SiGeSn	Silicon Germanium Tin
SIMS	Secondary Ion Mass Spectroscopy
SRH	Shockley Reed Hall Recombination
SRO	Shared Research Operations
TC	Thermocouple
UHV	Ultra-High Vacuum
VASP	Vienna Ab initio Simulation Package

XPS

X-Ray Photoelectron Spectroscopy

XRD

X-Ray Diffraction

CHAPTER 1: INTRODUCTION

1.1 Motivation

The future is here, and computation is king. Since the development of the first transistor, it is no understatement to say that the semiconductor was one of the greatest breakthroughs in modern science. Furthermore, just as scientists seek to further our species' knowledge, engineers seek to make things more efficient. As such, computational device speed, size, power dissipation, and a slew of other areas of interest have been the creative outlet for material scientists/engineers for the better part of the last century and into the modern era. Most everyone at this point has, at least in cursory fashion, heard of Moore's Law (Figure 1.1), the term used to refer to the observation made in 1965 by one Gordon Moore that the number of transistors in an integrated circuit will double every two years.

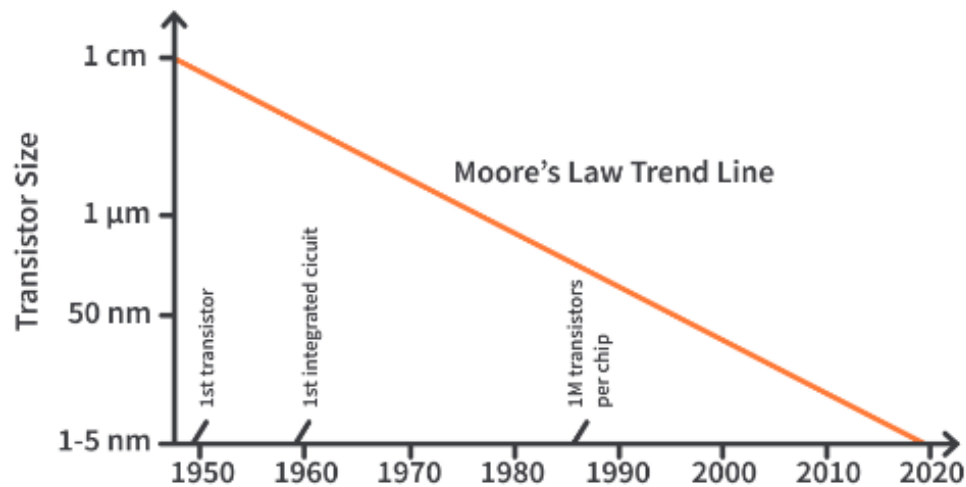


Figure 1.1: Moore's Law trendline [1].

Here, we can see a problem: what happens when transistors become too small as the effects of quantum tunneling begin to dominate? When will the density of transistors in a

circuit reach its limit? What happens when we need “*More than Moore*”? One possible answer to this, the primary focus of the Wistey group’s research, lies in the speed of light.

Due to the abundance of silicon and its overwhelming usage in modern electronics, Si-based monolithic lasers and other Si-based *photonic* devices remain highly desirable, because they would increase the speed of not only communication between chips, but even the types of computation we could do on each chip. Unfortunately for photonics, pure silicon joins its fellow Group IV elements (carbon, germanium, and tin) as an *indirect bandgap* material, which I will describe below. Indirect bandgap materials are incredibly poor light emitters, rendering them unusable for lasers and most other photonic devices. However, the study of germanium has caught fire again upon the realization that material engineering of new Ge alloys could make it a direct bandgap semiconductor suitable for lasers and other active photonic devices.

1.2 Route to Direct Bandgap Germanium

Long has it been the goal of many researchers [2] to achieve a direct bandgap Group IV material compatible with silicon CMOS devices. Direct bandgap silicon itself has been elusive for decades, as has device-ready direct bandgap germanium, at least at room temperature with realistic current densities. As it stands, tensile straining and alloying of germanium are the two routes commonly sought in changing the bandgap from indirect to direct (Figure 1.2). Indeed, several groups have shown promising results, both theoretically and experimentally, along both routes. He and Atwater showed that the optical energy gap of $\text{Sn}_x\text{Ge}_{1-x}$ should undergo an indirect to direct transition somewhere in the composition range of $0.15 > x > 0$ [3]. Others have x from 0.06-0.12 [4] [5],

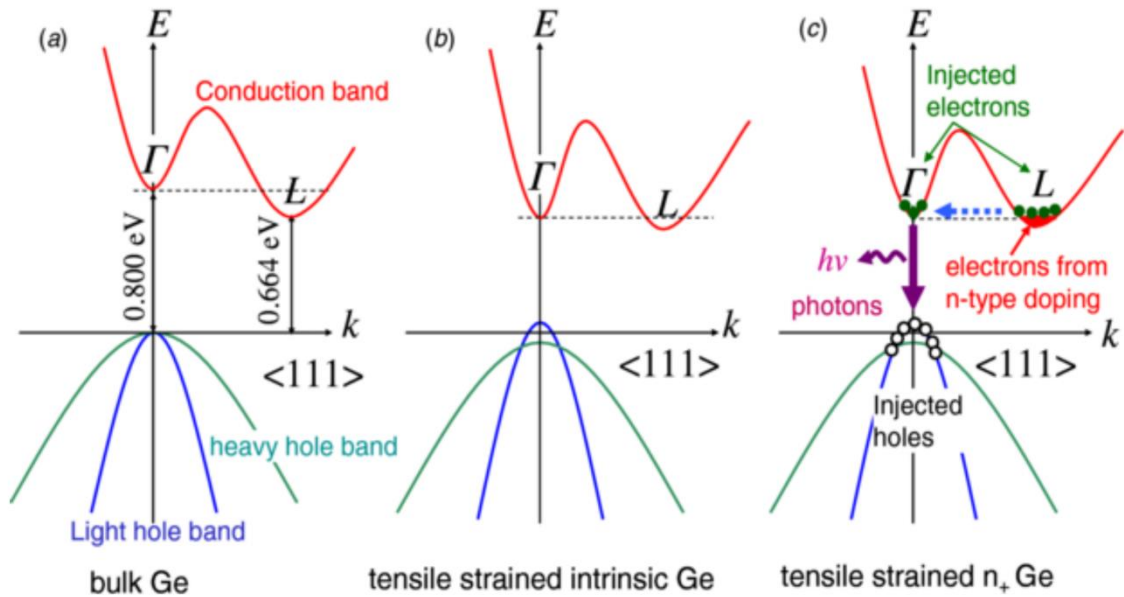


Figure 1.2: (a) Schematic band structure of bulk Ge, (b) schematic band structure of bulk Ge under tensile strain, (c) electron injection of Ge under tensile strain [6].

However, problems persist. The successful incorporation of up to 15% tin (Sn) into a germanium lattice has given rise to lasers, but these only operate cryogenically and with unreasonably high current densities [7]. Direct (or nearly direct) optical emission from tensile strained Ge (Figure 1.2 (b), (c)) has been reported, but the strain necessary to make emission efficient enough leads quickly to material dislocations and degradation [8].

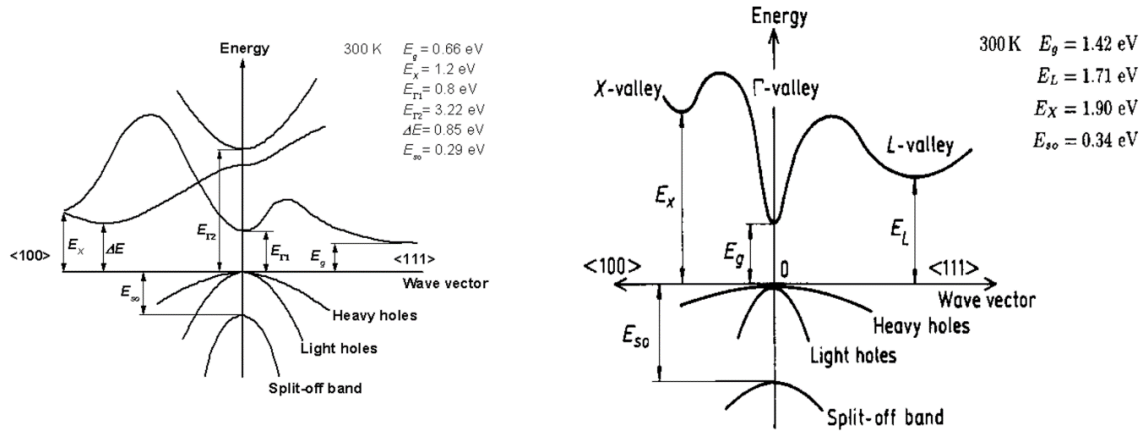


Figure 1.3: Sketches of the band diagrams for (a) germanium and (b) gallium arsenide. Arrows show direct and indirect bandgaps, respectively [9] [10].

The difference between the indirect and direct conduction band energy in germanium (Figure 1.3 (a)) is relatively small, on the order of only a few kT (136 meV) as seen in Figure 1.2, which is partly what makes it such a strong potential candidate for bandgap engineering. Alloying the germanium with substitutional carbon atoms creates dilute germanium carbide ($\text{Ge}_{1-x}\text{C}_x$, or simply GeC), a material studied extensively by our group both experimentally and computationally. Our group has shown through computational modeling that adding less than 1% C to Ge, forming the alloy GeC, can create a direct bandgap [11] by splitting the Ge conduction band into two separate bands, E^+ and E^- , whereby the E^- band shifts downward at the Γ -valley, creating a direct bandgap. Unfortunately, the solid solubility of C in Ge under thermal equilibrium would be much less than 1%, on the order of 0.001% ($\sim 1 \times 10^{18} \text{ cm}^{-3}$). Thus, growing quality GeC is challenging in that carbon prefers to bond to other carbons rather than to Ge, thus creating split interstitial defects. Our group previously has demonstrated successful growth of GeC with $\sim 1\%$ C using a special gas precursor, 4GeMe [12], to prevent these defects, but the 4GeMe molecule is challenging to synthesize on a large scale. Furthermore, the mismatch in size between Ge and C leads to high strain in the film,

leading to the generation of defects (dislocations) upon reaching the critical thickness.

Enter our novel material: GeSnC (germanium-tin-carbide). Alloying GeC with Sn offers multiple benefits:

1. Tin, being a larger atom than germanium, helps to compensate for the reduction in lattice spacing in the GeC structure, allowing for the growth of much thicker layers of GeSnC than comparable GeSn or GeC. Measurement techniques discussed later in this work describe why growing thicker layers are beneficial for material characterization.
2. GeSn can become a direct bandgap semiconductor at a ratio of roughly 6-11% [13] substitutional tin in the germanium lattice, depending on strain. Thus, even the addition of a small amount of Sn helps to drive GeC toward an even stronger direct bandgap.
3. Computational modeling by our group has shown that the bonding between Sn and C is more energetically favorable than that of two carbons forming an interstitial defect, which is critical considering that atomic substitution without defects is a necessity for most photonic devices.

Silicon as another substitutional candidate has yet to be incorporated into the growth process. Incorporation would offer device benefits such as a slightly wider bandgap, which may improve carrier confinement and ultimately be used as the cladding layer for a laser device.

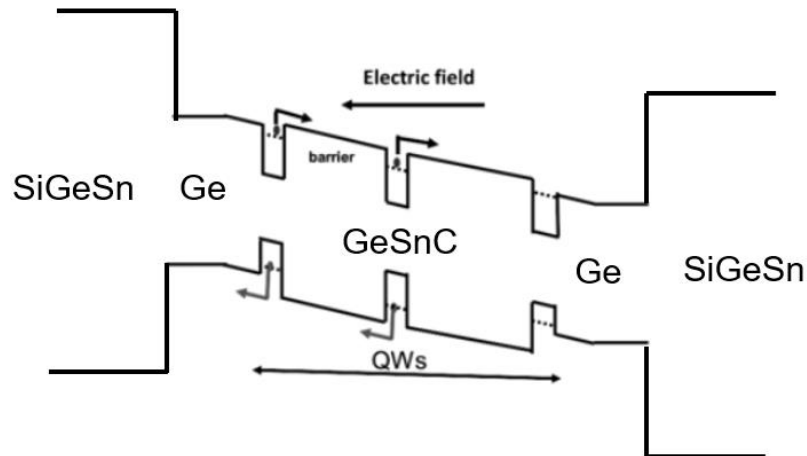


Figure 1.4: Band diagram of GeSnC heterostructure. Figure adapted from Wikiwand Quantum Well [14].

Ultimately, we seek to demonstrate direct bandgap GeSnC monolithically grown on a silicon substrate to replace low-yield, wafer-bonding methods that are currently being used to patch direct bandgap materials such as GaAs onto silicon [15]. That the GeSnC alloy is so close in composition to germanium is key, as germanium has been shown to be grown monolithically on silicon without defects [16]. Plus, finding an active material that can compete with GaAs (the industry-standard direct bandgap material) would alleviate the need for toxic arsenic problems with possible contamination of semiconductor fabrication facilities.

1.3: GeSnC Quantum Wells

The properties of semiconductor heterostructures have been exploited for their use in modern electronics for decades. The heterostructure, a term that simply refers to two separate and distinct semiconductor materials coming in direct contact with one another, is the foundation of many advanced electronic devices, optical devices, and optoelectronic devices, and earned a Nobel prize [17]. Our group uses a growth technique known as molecular beam epitaxy (MBE) that can easily switch between materials to

grow heterostructures, and it can grow GeSnC alloys on either germanium or gallium arsenide substrates. Figure 1.4 depicts a potential band diagram for such a structure.

Arguably the most important heterostructure is a quantum well (QW), which is a sandwich of two heterostructures back-to-back to confine electrons and/or holes in a layer that is only a few nanometers thick. QWs are the cornerstone for devices like lasers, amplifiers, and modulators. QWs are particularly desirable due to their underlying physics being closely adapted from the particle-in-a-box model, thereby acting as carrier confinement centers [18]. Thus, this work reports on the growth and characterization of multiple quantum wells (MQW) formed from alternating layers of Ge/GeSnC/Ge.

1.4 Growth and Characterization: Bulk and MQW Heterostructures

I grew GeSnC using our group's Intevac Gen-II MBE system with hybrid sources: Multiple techniques have been used to characterize these materials under the Analysis Research Service Center (ARSC) at Texas State University under Dr. Casey Smith. Other characterization external to our department has been carried out by two groups we work closely with. Dr. Seth Bank and Dr. Aaron Muhowski at the University of Texas at Austin performed the photoluminescence (PL) and secondary ion mass spectroscopy (SIMS) measurements. Dr. Rachel Goldman's group at the University of Michigan at Ann Arbor performed the Rutherford backscattering spectroscopy (RBS).

1.5: Summary

This thesis is divided into the following parts: Chapter 2 explores the background and work I completed alongside the other growers in the group to grow bulk C- or Sn-alloyed Ge. In chapter 3 I show how I translate my knowledge from bulk growth into MQW growth and touch on some characterization techniques used in this work. Chapter

4 focuses on the fixes made to the growth process with proven increase in material quality and finishes out with my particular focus in the optical characterization of both bulk and MQW GeSnC samples. Chapter 5 will present the summary of the thesis work done and the scope of future research. The Appendix will include auxiliary projects, as well as other pertinent information regarding this work.

CHAPTER 2: BULK EPITAXIAL THIN FILM GROWTH AND CHARACTERIZATION

2.1 Molecular Beam Epitaxy

Molecular beam epitaxy (MBE) is a process by which high-purity epitaxial (crystalline growth) layers of semiconductor can be grown in an ultra-high vacuum (UHV) environment. While there are myriad ways of achieving high-quality growth of semiconductors (for example, liquid-phase epitaxy (LPE) and chemical vapor deposition (CVD)), the advantages offered by MBE come from the ability to fine-tune the deposition rate and to switch abruptly between different materials, the ultra-high vacuum (UHV) environment that prevents contamination, and real-time feedback from in-situ RHEED monitoring, as seen in figure 2.1. Our solid sources (germanium, tin, and gallium) are kept near their melting point as solids in their respective crucibles in Knudsen effusion cells. Once we are ready to grow, we heat these cells to a desired temperature, utilizing Eurotherm PID controllers and feedback loops with Sorenson DC power supplies and thermocouple temperature monitors, to produce various fluxes that we measure with our beam flux monitor (BFM). Unless otherwise specified, all temperatures reported in this thesis are thermocouple temperatures. Please see Tuhin Dey's Ph.D. dissertation for calibration of actual wafer temperatures.

Furthermore, our MBE is equipped to use gas precursors in our growth sequences. Gas-source MBE is more difficult to control than solid-source, but through software and mechanical modifications I have recently achieved reliably constant BFM readings.

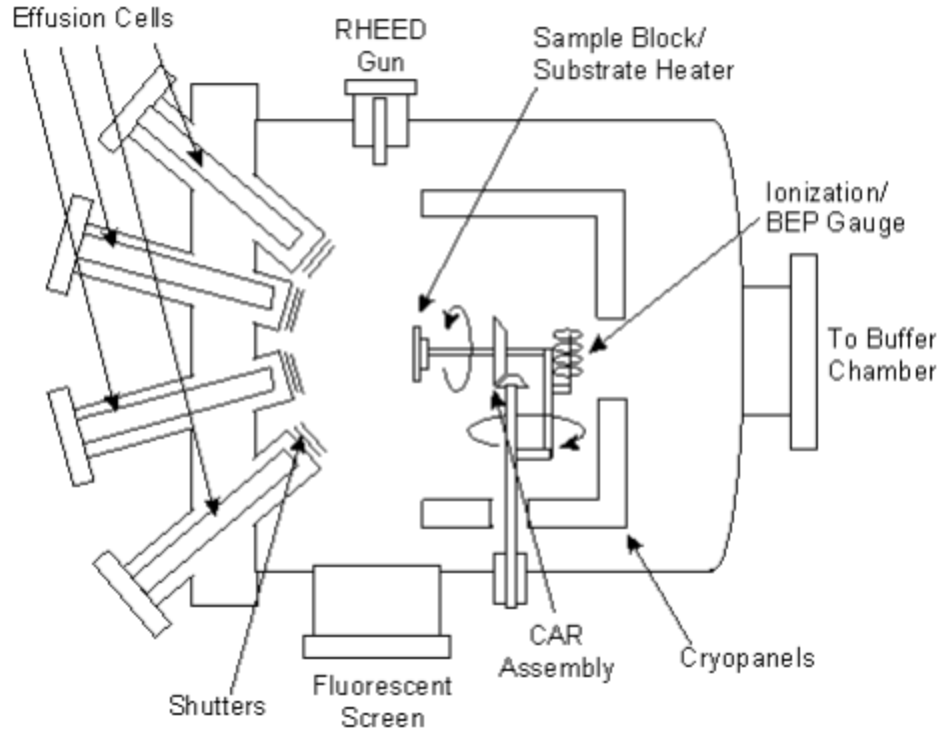


Figure 2.1: Varian Gen-II MBE system [19].

Impurity-free and UHV environments are essential in any successful MBE machine. To achieve this, our chamber is outfitted with an ion pump, a scroll pump-backed Pfeiffer turbomolecular pump, and a titanium sublimation source. When the gate valve to the turbo pump is closed, the ion pump will keep the chamber down in the 1×10^{-9} Torr pressure regime, however often it is the case that we wish to use both pumps simultaneously. The turbo pump also utilizes nitrogen as a purge gas to keep its bearings clean from corrosive gases during operation. We monitor the vacuum environment using a residual gas analyzer (RGA), i.e. a mass spectrometer. We try to not use the RGA too much, as the hot filament can burn out (especially during growths that use gases at higher pressure), but it offers us a way to gauge exactly what is in our chamber at the different stages of our growth and after maintenance openings.

The MBE we use is one of the two owned by the Wistey group: one dedicated to the growth of Group IV semiconductor materials, and the other to III-V materials. The III-V chamber is named “Firehole” (Figure 2.3), and contains effusion cells for Ga, In, Al, As, Sb, P, and Ge. The Group IV system is named “Green” (Figure 2.2) and is outfitted with solid source Ge, Sn, and Ga, an atomic hydrogen cell, a BandiT camera and shutter setup for finer wafer temperature monitoring, two gas injectors, and one effusion cell with an empty pyrolytic boron nitride (PBN) crucible for p-type boron doping.

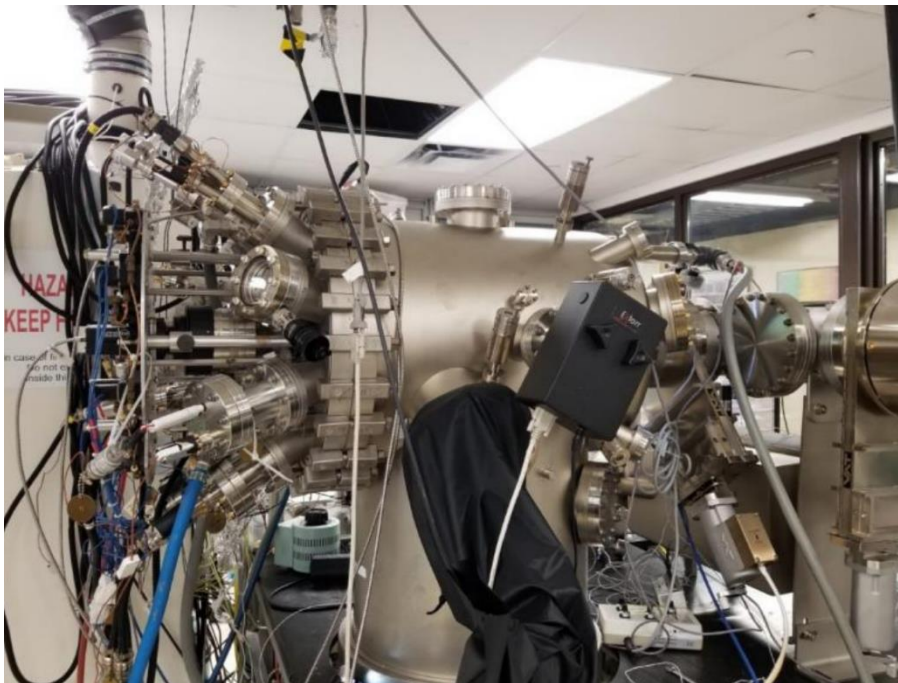


Figure 2.2: Wistey Group Varian Gen-II Group-IV MBE system [5].

Our MBEs are connected by a buffer chamber kept at UHV pressures by two separate ion pumps. Typically, the cleanest part of our entire system (pressures in the 1×10^{-9} or 1×10^{-10} Torr regime), it is here we store both already-grown wafers and wafers on which we wish to grow on one of two moveable trolleys. The two trolleys are moved throughout the buffer and loading stations using magnet coupling on a physical track. Each individual section is separated by a gate valve, which helps especially when trying

to isolate a particular area when either performing leak checks or the repair/maintenance of the equipment.

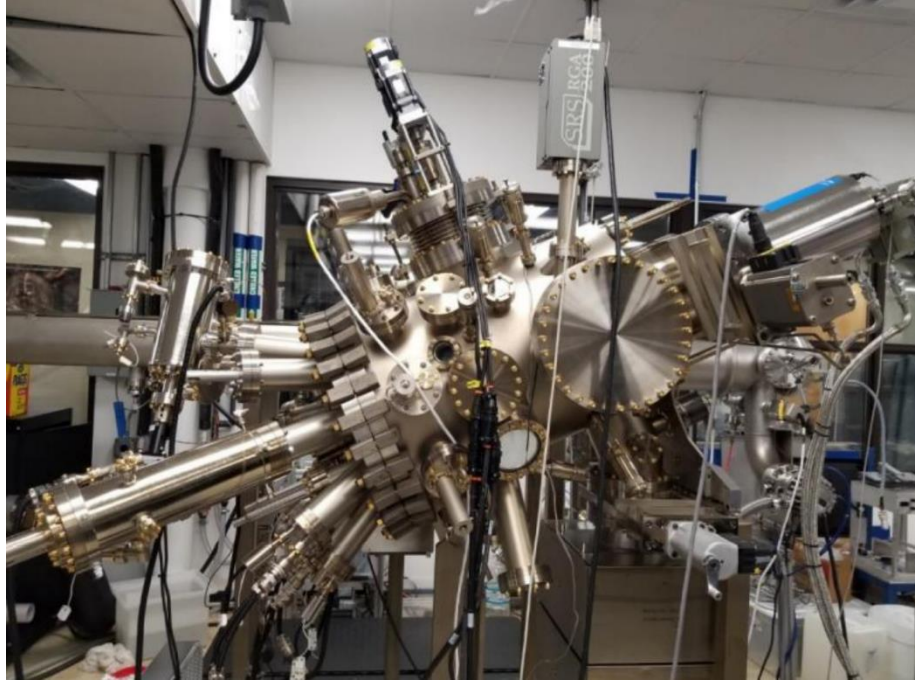


Figure 2.3: Wistey Group Veeco Gen 930 III-V MBE system [5].

Until as recently as Fall 2021, the growths on the Group-IV machine were controlled manually. Now, the MBE system is outfitted with the software package Molly, one of the standard MBE real-time control software, that can control everything from the heating of the cells to the rotation of the manipulator and opening of the cell shutters. While it would have been possible to have grown the quantum wells manually, the incorporation of Molly greatly enhanced the control of my MQW growths. Indeed, the first growth I ever completed on this machine was also the first use of Molly for machine control. Up until that point, all growths by my colleagues were done manually.

2.2 Bulk Germanium

Bulk germanium and GaAs have remarkably similar relaxed lattice constants, 5.658 Å for germanium and 5.653 Å for GaAs, a difference of 0.088%. This gives us the

ability to grow very thick layers of germanium atop GaAs without risk of reaching the critical thickness where strain relaxation would create dislocation defects [20]. Thus, the growths my colleagues and I first completed at Texas State were our most simple: a Ge epitaxial lattice on a GaAs substrate. These growths served two purposes: 1) Good first practice with the MBE growth technique, 2) germanium growth-rate calibrations. The optimization of Ge growth is one of many critically important steps towards successful device fabrication.

The desired growth rate of germanium in our system is 100 nm of material/hour. The beam equivalent pressure (BEP), as measured by the BFM, was found to be 1.61×10^7 Torr and verified using the SRO's Surface Profilometer by growing Ge at this flux for ten hours on GaAs, after which I measured the depth profile (height) of the grown sample with respect to a part of the wafer that was covered up during growth. This flux was produced when the germanium cell was at a temperature of around 1250 °C, though this temperature will vary as the solid source material runs out. As will be discussed when it comes to quantum well thicknesses, the deposition rate is critical. Simply put, if more or less material is desired, raise or lower the temperature of the cell.

If grown too cold, Ge growth – or any epitaxial growth – can enter the statistical growth regime, wherein any germanium atom has a higher probability of simply sticking where it hits the surface of the epi layer and not finding an optimal crystal lattice site. This can be disastrous for devices we wish to fabricate, as it creates many defects, particularly crystal vacancies. Through our efforts, it was determined that the highest quality germanium should be grown at a CAR thermocouple (TC) temperature of at least 380 °C for our system. Germanium can be grown well at temperatures far exceeding this

[21], however the colder temperature prevents degradation of the GaAs substrate during growth.

2.3 P-Type Doping, Ge:Ga

X-Ray Photoelectron Spectroscopy (XPS), done by Tuhin Dey, and Time-of-Flight Secondary Ion Mass Spectroscopy (ToF-SIMS), done by Seth Bank's group at The University of Texas at Austin revealed arsenic contamination through the epi-layers of each of our samples grown on GaAs substrates until as recently as late 2021. We had been growing our Ge buffer layer too hot, causing the degradation of the surface of the GaAs substrate, thus allowing for broken-bonded arsenic to either diffuse up or ride the growth front and infiltrate the epi, causing unintentional n-type doping of our growths. As I will discuss later, there was no photoluminescence (PL) from these samples. This makes sense in hindsight; doping creates a built-in electric field that separates electrons and holes before they can recombine to emit light. To counteract this effect, I have taken the approach of doping the germanium buffer layer we grow atop the GaAs substrate with gallium, which is a p-type dopant that will compensate for any remaining n-type arsenic doping.

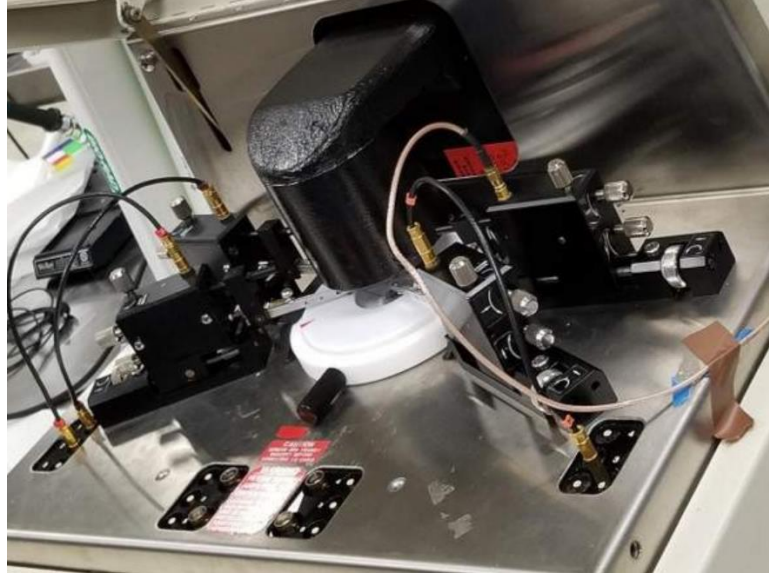


Figure 2.4: Texas State SRO Bio-RAD Hall measurement system (courtesy of TXST SRO).

To calibrate our doping, I grew six doping growths: three separate doping concentrations, all on both 1- μm - and 2- μm -thick Ge on GaAs. Estimates for carrier concentrations were done using the Arrhenius model, similar for what we use for taking source material fluxes, and then verified by Hall measurements using the Texas State SRO's Bio-RAD Hall measurement system (Figure 2.4). Doping concentrations were loosely estimated by

$$\frac{flux_{Ga}}{flux_{Ge}} = \frac{Concentration_{Ga}}{Concentration_{Ge}}$$

where we sought hole concentrations of 1×10^{16} , 1×10^{18} , and 1×10^{20} holes/vol³. I measured the resulting growths in the Bio-RAD Hall measurement system by cleaving two samples from each into 5mm \times 5mm squares, melting indium dots onto each of the surfaces' four corners and loading them onto the probe station. The settings for the measurements maximized for allowed voltage and current, with typical voltage ranges of 1-2 V and 7-20 mA, and each sample showed a strong ohmic relation within its respective setpoints.

Table 2.1: Doping concentrations for various thickness Ge:Ga. Sign denotes measured carrier charge (-) (+).

Thickness (um)	Expected Concentration	Measured (carriers/cm ³)	Surface Measured (carriers/cm ²)
1	1.00E+16	-8.00E+17	-8.00E+13
1	1.00E+18	-8.63E+17	-8.63E+13
1	1.00E+20	1.54E+20	1.54E+16
2	1.00E+16	-8.40E+17	-1.60E+14
2	1.00E+18	1.60E+18	3.19E+14
2	1.00E+20	1.20E+20	2.40E+16

With this data, it was determined that I should shoot for a 1×10^{18} carrier concentration in my buffer layers atop GaAs substrates, because it would be high enough to compensate the highest n-type doping in any of our samples.

The growth dynamics and integration of Ge-on-GaAs offers yet another challenge: If the native surface oxides are desorbed at too high a temperature (400 °C and up) under a steady flow of atomic H, we believe the hydrogen will remove a percentage of the surface arsenic, creating the opportunity for the leftover gallium atoms to find each other on the surface and form gallium droplets. This uncovers more arsenic underneath, and the cycle continues. A flat epi-ready surface is desirable for MBE growth and these gallium droplets can be the cause of a growth going bad.

2.4 Bulk $Ge_{1-x}C_x$ and $Ge_{1-y}Sn_y$

2.4.1 Gas Precursors: Carbon Tetrabromide and Hydrogen

The two materials used in the growth of our dilute germanium carbide ($Ge_{1-x}C_x$) are solid source 6N pure Ge and gaseous carbon tetrabromide (CBr_4). As mentioned in the introduction, carbon-carbon bonds are one of the key material issues we are trying to avoid. A carbon atom tetragonally bonded to four bromine atoms offers one such solution to this problem under certain growth conditions. Hybrid MBE systems such as ours offer their benefits and challenges, and one such challenge is the fine control needed for

gaseous precursors. Considering that the MBE environment is always under UHV conditions and that growth conditions can vary immensely with slight changes in fluxes and temperature, the control of a steady gas source is paramount for high quality material.

CBr_4 (see Figure 2.5 for molecule schematic) is a sticky gas with a low vapor pressure. As such, it wants to stick to the walls of the gas lines leading to the growth environment and can cause build-up to the point that renders the lines useless. To prevent this issue, we lined the entirety of the gas lines comprising the gas cabinet with heater tape which acts to keep the lines too hot for our precursors to stick to.

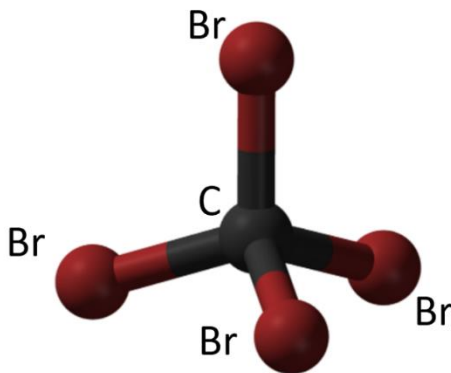


Figure 2.5: Carbon tetrabromide molecule [22].

We use the combination of a computer-controlled leak valve, a needle valve, two pneumatic valves, an all-metal valve, and a shutter to control the beam equivalent pressure as read by the BFM, as well as two Baratron in the gas cabinet to monitor pressures in the cabinet. That the Baratron read a constant pressure during growth is an indication that we have a steady, consistent flow of gas.

One more addition I made to the system was the building and installation of our hydrogen purifier (see Appendix for details). The purifier lines introduce 8N pure hydrogen into our atomic hydrogen cracker which splits H_2 atoms into their monatomic constituents at a rate of approximately 1-in-10 atoms split per volume. This, too, is

controlled by a pneumatic valve, an all-metal valve, and a shutter.

Another gas precursor deserves mention here: tetragermymethane (Figure 2.6), or $(\text{GeH}_3)_4\text{C}$ (or, colloquially, 4GeMe). As mentioned, getting the carbon atoms to properly substitute for Ge atoms is necessary for photonic devices, and this molecule offers just that: a carbon surrounded by four sp^2 -bonded germaniums with hydrogens attached to the outside of each germanium atom. Implemented previously by Dr. Wistey at Notre Dame, we are seeking a way to develop this precursor again for use in our system.

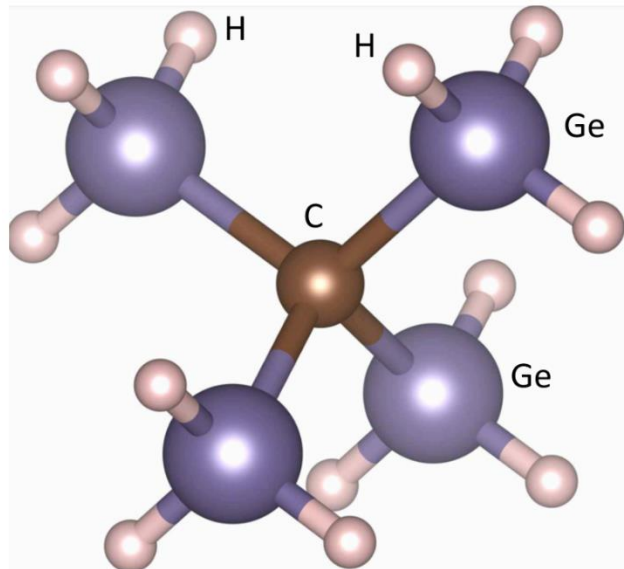


Figure 2.6: Tetragermymethane (4GeMe) molecule [12].

2.4.2 $\text{Ge}_{1-x}\text{C}_x$

I worked closely with Shamim Reza, whose Ph.D. research was on the growth and characterization of dilute $\text{Ge}_{1-x}\text{C}_x$. This growth series, for which I grew some of the samples, found that without the presence of ambient atomic hydrogen the carbon percentage varies by ten percent over the CAR TC temperature range from 215-324 °C , the highest y-value not to exceed 0.79%. The best crystal quality, shown in Figures 2.7 and 2.8, as determined by reflection high energy electron diffraction (RHEED), atomic

force microscopy (AFM), and XRD was found to be in the lower limits of the temperature regime with the best at 215 °C.

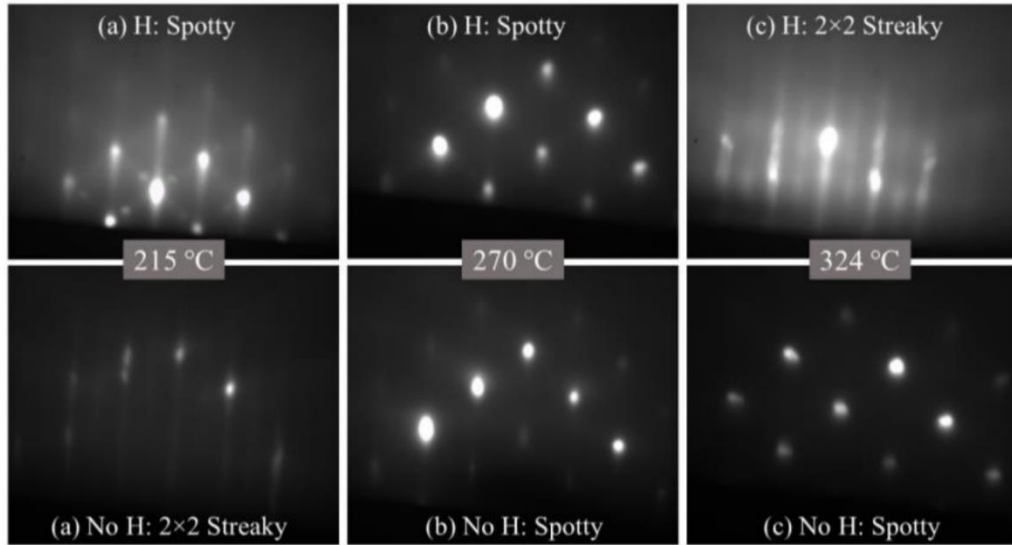


Figure 2.7: (a)-(c) RHEED images of samples grown under atomic-H at 215 °C, 270 °C, and 324 °C, respectively. (d)-(f) RHEED images of samples grown without atomic-H at 215 °C, 270 °C, and 324 °C, respectively. Streaky RHEED indicates smooth surface [5].

Interestingly, there is however a pronounced inverse effect from the presence of hydrogen, where it was found that the best quality thin film growth was achieved at the upper limits of the temperature regime. It appears that H_1 increases the fraction of C incorporated substitutionally in Ge. Furthermore, substitutional carbon in the germanium lattice has been confirmed by Tuhin Dey and Dr. Shamim Reza [5] [23].

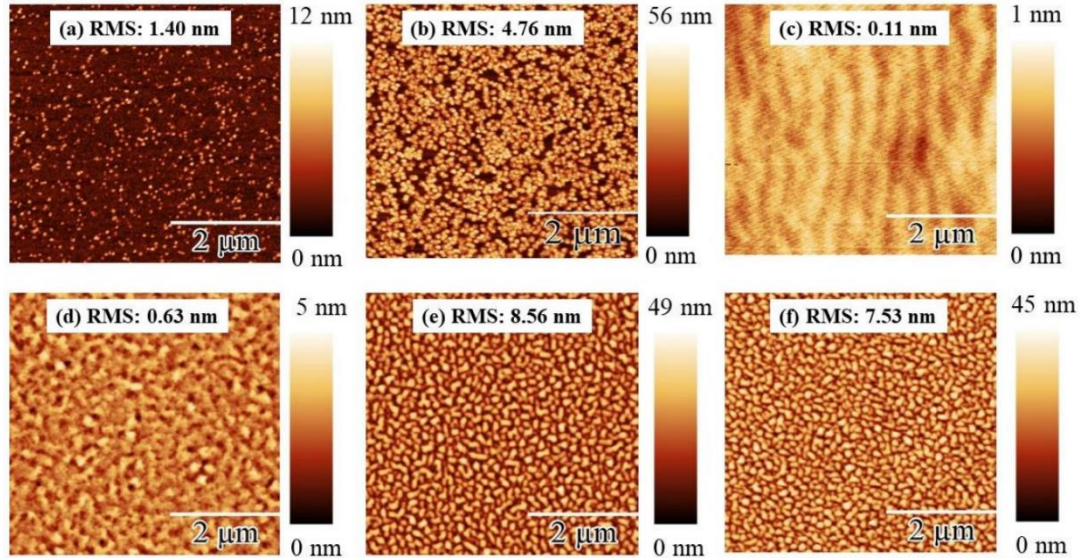


Figure 2.8: (a)-(c) $5 \times 5 \mu\text{m}^2$ AFM images of samples grown under atomic-H at 215 °C, 270 °C, and 324 °C, respectively. (d)-(f) $5 \times 5 \mu\text{m}^2$ AFM images of samples grown without atomic-H at 215 °C, 270 °C, and 324 °C, respectively [5].

2.4.3 $\text{Ge}_{1-y}\text{Sn}_y$

Tuhin Dey's ongoing Ph.D. research complements Dr. Shamim Reza's by adding Sn. The Sn flux is more easily managed than its gaseous carbon counterpart because Sn is provided by solid evaporation source. RHEED, AFM (Figure 2.9), and XRD reveal that the best temperature at which to grow $\text{Ge}_{1-x}\text{Sn}_x$ ($x = 0.004$) is 180 °C.

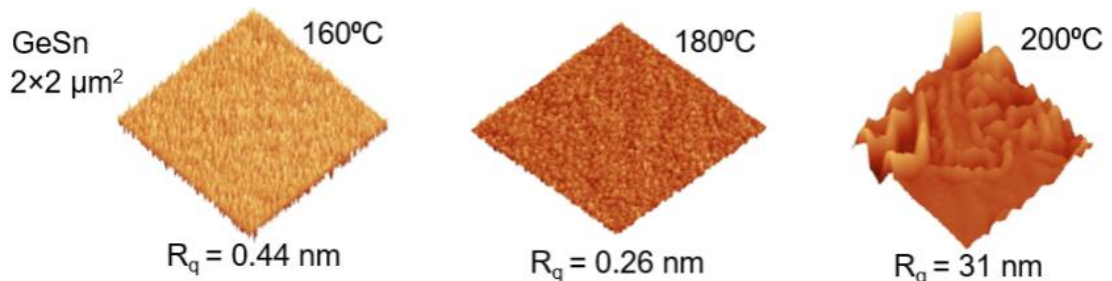


Figure 2.9: (a)-(c) $2 \times 2 \mu\text{m}^2$ AFM images of GeSn samples grown at 160 °C, 180 °C, and 200 °C, respectively [23].

2.5 $\text{Ge}_{1-x-y}\text{Sn}_x\text{C}_y$

The foray into bulk Ge growth with small amounts of C or small amounts of Sn has been with the goal of creating the dilute $\text{Ge}_{1-x-y}\text{Sn}_x\text{C}_y$ alloy. As previously mentioned,

the addition of both C and Sn in the Ge lattice are wedded in their effect of shifting the band gap of Ge to become more direct, each in their own characteristic way. Tuhin recently showed successful growth of this material [23].

Following from the previous two sections, this material shows the following characteristics:

1. XRD (Figure 2.10) shows all layers are atomically aligned and strained (pseudomorphic) to the GaAs substrate with high crystal quality.
2. Raman spectroscopy has verified that carbon is going into the lattice substitutionally with no alternate C or Sn phases.
3. AFM (Figure 2.11) shows the sample with the highest C and Sn concentration to have an atomically flat surface.
4. Scanning electron microscopy (SEM), optical microscopy, and AFM all show no surface Sn droplets, which are a common problem in GeSn growth.

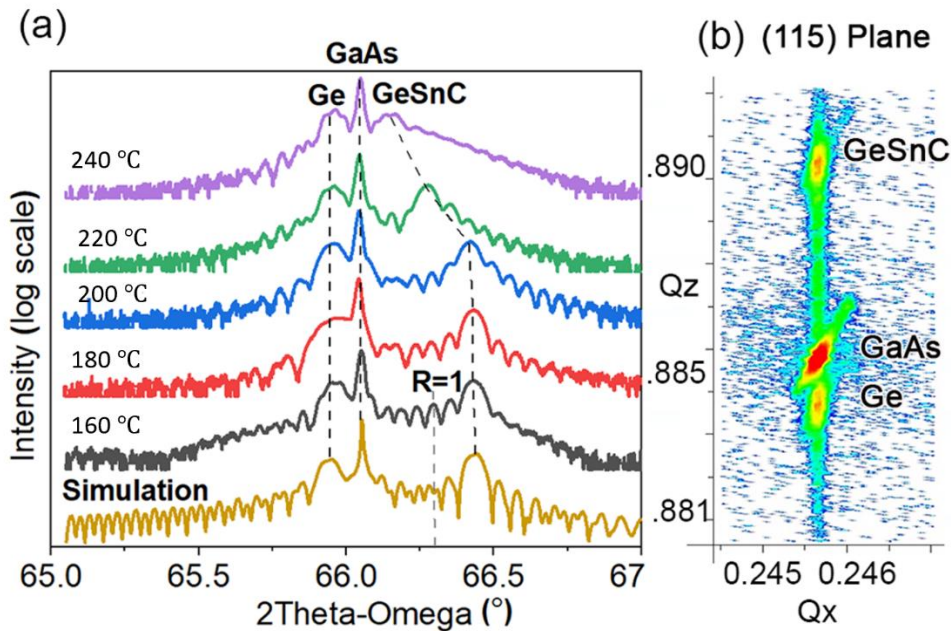


Figure 2.10: (a) $\text{Ge}_{1-x-y}\text{Sn}_x\text{C}_y$ HR-XRD 2Theta-Omega scans about (004), (b) RSM around (115) plane for the 160 °C sample [23].

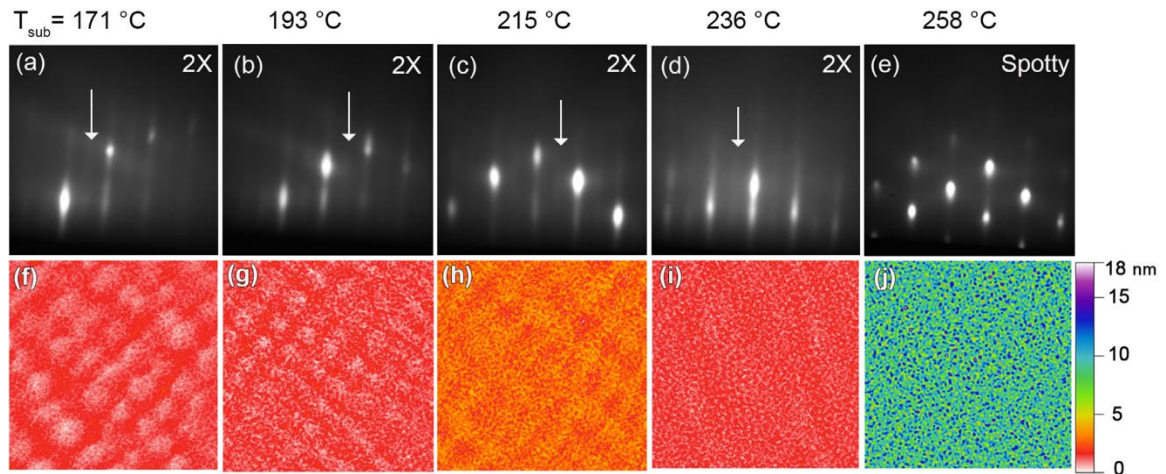


Figure 2.11: (a)-(e) RHEED for $\text{Ge}_{1-x-y}\text{Sn}_x\text{C}_y$ growths at various temperatures. 171-236 °C show smooth surfaces (streaks) with 2× surface reconstruction, but highest growth temperature (258 °C) shows spots indicating rough growth. (f)-(i) AFM scans over $2 \times 2 \mu\text{m}^2$ of same samples, indicating atomically flat surfaces except at 258 °C [23].

To get absolute compositions of the Sn and C, we sent samples to Dr. Rachel Goldman's group at The University of Michigan at Ann Arbor for Rutherford backscattering spectroscopy (RBS). Nuclear reaction analysis RBS (NRA-RBS) is necessary to measure small atoms like C, which complicates the technique. As of this writing, we are still waiting for definitive RBS and NRA-RBS results, but preliminary measurements suggest our C and Sn content to both be on the order of 1% for most samples.

CHAPTER 3: MULTIPLE QUANTUM WELL EPITAXIAL THIN FILM GROWTH AND CHARACTERIZATION

3.1 First MQW Growth: GeSnC/Ge on Semi-insulating GaAs Substrate

This project began because of our new capacity to automate growths in our MBE system, as far as it was viable. The wafer-loading, heating, and desorption, for instance, still need to be done manually, but once the growth is started, the main controls needed can be written in code steps via Molly. The most important controls are CAR TC temperature, wafer rotation, cell and gas shutters, and timing. A typical growth of a MQW sample, depending on buffer thickness and desired number of wells and barriers, can range from six to twenty hours.

My first-ever growth consisted of 25 GeSnC QWs with Ge barriers between them, grown on a 300 nm undoped Ge buffer, which itself was grown on a non-intentionally doped (semi-insulating) GaAs substrate (see Figure 3.1). The wells were 5 nm thick, and the barriers were ~19 nm thick.

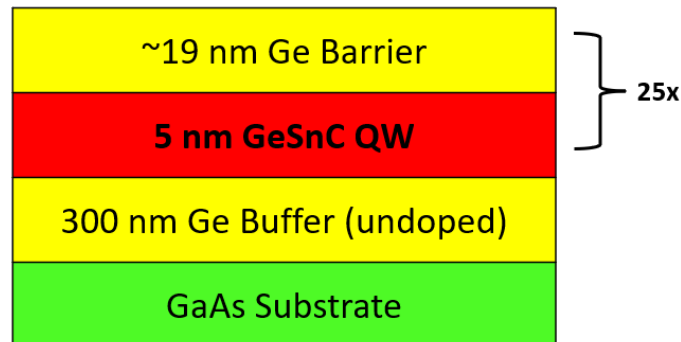


Figure 3.1: First GeSnC/Ge MQW heterostructure, grown on semi-insulating GaAs.

The growth rate for the germanium cell was 100 nm per hour, requiring 3 hours of growth for the buffer and 3 minutes and 11.2 minutes for the wells and barriers, respectively. The CAR TC temperatures were 390 °C for the buffer and 190 °C and 390

°C for the wells and barriers, respectively. Some of Tuhin's and Shamim's growths were performed under a beam of thermally cracked hydrogen, and the H cell heats the wafer by roughly 5 °C above that suggested by the TC. To prevent temperature variation between growths (and growers!), the group collectively agreed the atomic hydrogen source would also be at full power (8.5 A filament current) with its shutter open, but with no H₂ gas. Therefore, the final growth temperatures are assumed to be 395 °C for the buffer and 195 °C and 395 °C for the wells and barriers, respectively. We did not have our other temperature monitor, BandiT, up and running at that time, so we had less accurate temperature monitoring.

Control of the temperature on the CAR for the two different phases of growth, QW and barrier, is managed by the PID feedback on the Eurotherms. This first MQW sample was grown with the PID settings mistakenly auto tuned for the higher TC temperature, 390 °C. As a result, the QW temperature oscillated wildly during its growth, with the CAR heater's Eurotherm alternating between full and zero power. As will be seen by the XRD measurements later, the crystal quality was not as high as future growths of the same sample, perhaps in part for this reason. The heating/cooling cycles from barrier to QW and back were also controlled somewhat crudely by timing rather than awaiting a certain condition to be met in the growth recipe on the computer. This could explain poor crystal quality as well because it takes around four minutes to heat the CAR from well to barrier temperature, and when GeSnC sits too long at excessively high temperature, the probability of tin and carbon segregating and "riding" the surface and creating unwanted bonds increases, which is another possible explanation for poor crystal quality. Further studies are needed on annealing treatments of GeSnC, particularly with

this in mind for MQW samples. Furthermore, the twenty-six-minute cooling period to reach QW temperature was later determined to have been underestimated by ten minutes, resulting in a hotter growth than was prescribed.

3.2 Characterization

3.2.1 RHEED

Reflection High-Energy Electron Diffraction (RHEED) is a standard setup in many MBE (and other UHV) growth systems. RHEED is most useful for *in situ* determination of how flat and uniform a growth surface is. We use a setting of 10 kV and 1.5-1.55 mA filament current to power the electron gun that, when powered and allowed to probe the surface by opening the shutters to both the gun and the phosphorous-coated detector

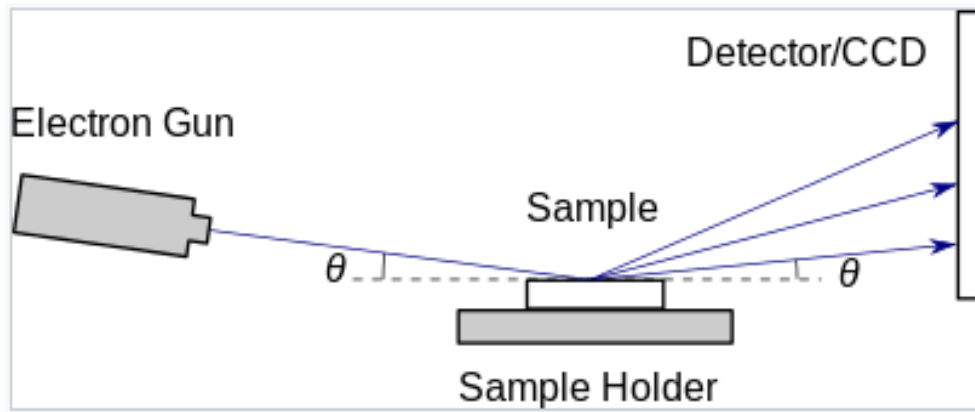


Figure 3.2: RHEED Diagram [5].

screen, fires high-energy electrons that will diffract at angles associated with the sample's atomic crystal structure as depicted in Figure 3.2. A camera is placed in front of the phosphorous screen for image capture. RHEED offers an excellent first-glance at how a growth is proceeding.

3.2.2 X-Ray Diffraction

X-Ray diffraction (XRD) is one of the most important tools in the material scientist's belt. Postulated originally by Sir William L. Bragg, and his father, Sir William H. Bragg, Bragg's law:

$$n\lambda = 2d\sin\theta$$

Earned a Nobel prize for the duo. d represents the distance between atomic layers in a lattice (z-direction in this case), θ is the light beam incident angle, λ is the wavelength of light, and n is an integer (Figure 3.3). The physical principle is that the lattice effectively acts as a three-dimensional diffraction grating, where each diffraction spot is related to the reciprocal lattice created by periodic crystal planes. Two of the most common measurement techniques are reciprocal space mapping (RSM) and rocking curve measurements.

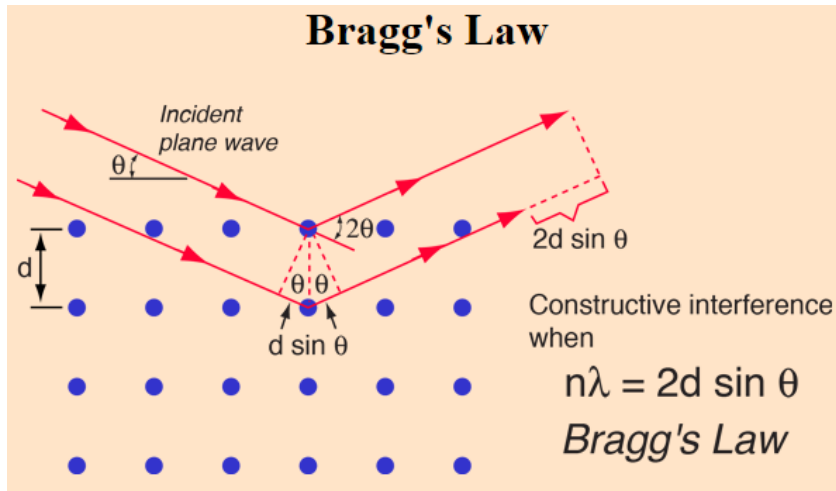


Figure 3.3: Bragg's Law diagram [24].

This measurement technique is incredibly useful, and it has been used by our group in a few ways:

1. Calculating relative alloy percentages based on z-direction strain.
2. Crystal quality as determined by appearance of Pendellösung fringes.

3. RSM measurements to verify lattice-matching to GaAs and Ge substrates.

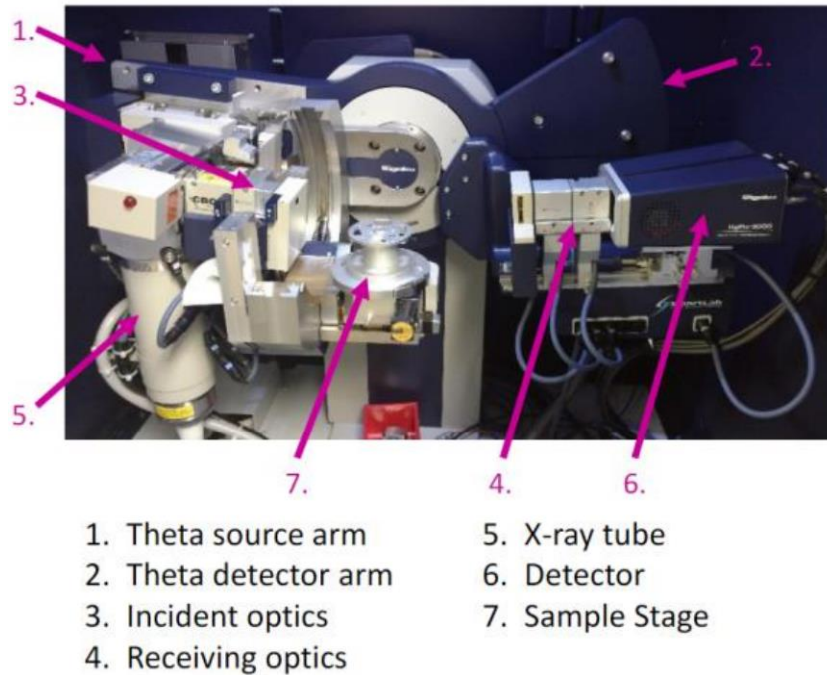


Figure 3.4: Texas State SRO Rigaku XRD system (courtesy of TXST SRO).

In addition, we can perform rocking curve measurements around a particular assumed angle (typically that of the expected GaAs diffraction angle, $\omega = 66.07^\circ$) by $\pm 1^\circ$ to maximize the results of the 2Theta-Omega scan.

A 2Theta-Omega scan was performed by me using the SRO's Rigaku XRD system (Figure 3.4) for the first quantum well sample I grew. The highest and sharpest peak is that of the GaAs substrate, and the left-most of the three middle peaks is from the Ge buffer. This leaves the middle-most peak, which represents the $\text{Ge}_{1-x-y}\text{Sn}_x\text{C}_y$ (Figure 3.5). The lack of Pendellösung indicates poorer crystal quality than desired, but the inclusion of the peaks to the right and left provides evidence of distinguishable quantum well structures existing in the lattice. In addition, the close spacing of the alloy peak to both the Ge and GaAs peaks indicates that it is closely lattice-matched to these layers.

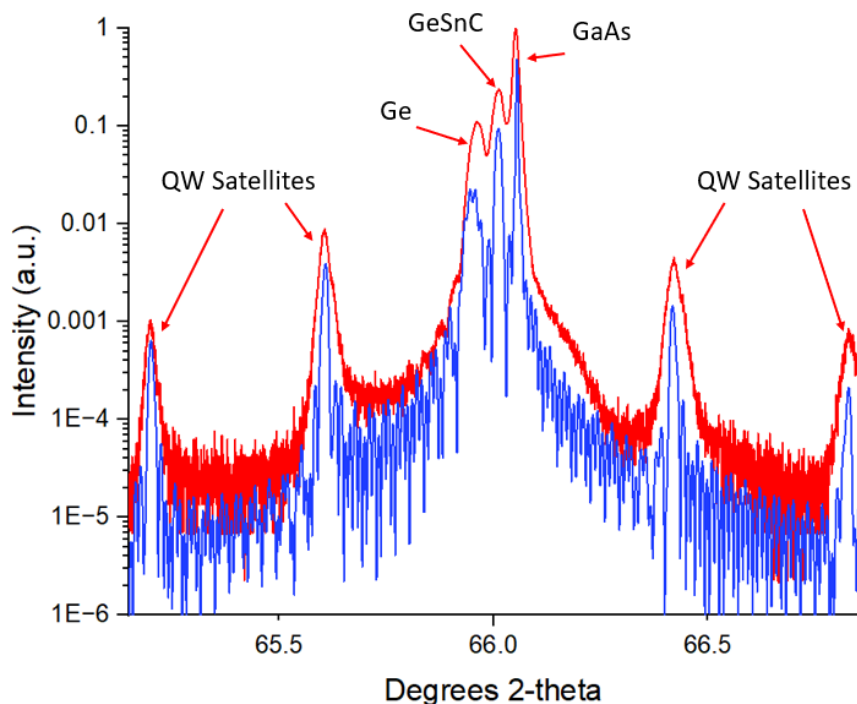


Figure 3.5: 2θ - ω XRD scan of first GeSnC/Ge MQW on GaAs substrate (red), GlobalFit simulation peak-fit (blue).

Global Fit software was used to try and match peaks to determine the concentration of substitutional Sn and C in the lattice. The software reported a fit of 2.6% Sn and 1.75% C, but these compositions are far too high based on recent XPS and RBS measurements of similar bulk samples. However, it is fair to conclude that the Sn:C ratio in our sample is roughly 1.5:1. Furthermore, if C and Sn are allowed to vary in the simulation, the software can converge at multiple values with the same distance between QW satellite peaks, further justifying the need for a more rigorous way of quantifying alloy percentages.

3.2.3 Photoluminescence

Photoluminescence (PL) is the most important and relevant measurement tool for our material, since it measures actual emitted light, which is our primary goal. The total emission from the first MQW sample was measured using a micro-PL setup by Dr. Aaron

Muhowski at UT Austin.

For PL, the sample is held in a temperature-controlled cryostat with a ZnSe window. The sample was optically pumped by a 1 W laser operating at a wavelength of 808 nm, modulated at 10 kHz. The pump laser light was passed through a 3 μm dichroic beam-splitter and focused onto the sample using an all-reflective objective. PL emitted from the sample was collected by the same objective and reflected by the dichroic beam-splitter. The reflected light was focused by a reflective parabolic mirror through an AR-coated (3–5 μm) Si window onto a liquid nitrogen cooled InSb photodetector. The Si window was used to filter out laser light. The detector signal was demodulated by a lock-in amplifier and recorded for each temperature of the sample. For spectrally resolved photoluminescence measurements, infrared light was passed into a Fourier transform infrared (FTIR) setup after being reflected from the dichroic. The FTIR was run in the step-scan mode to dramatically reduce infrared background. The input power was approximately 240 mW, focused into an ellipse of $200 \times 40 \mu\text{m}^2$.

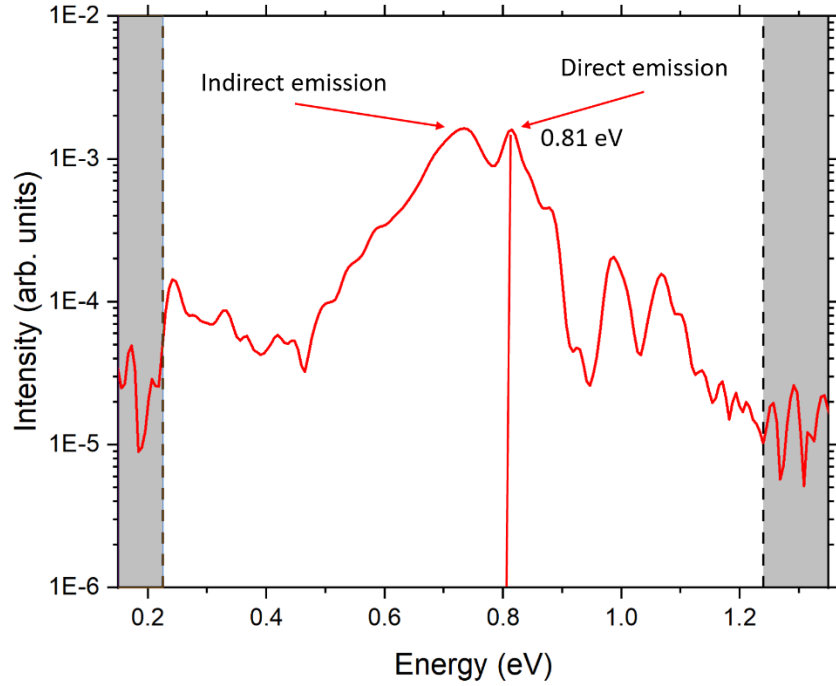


Figure 3.6: Photoluminescence of first MQW sample.

The photoluminescence measurement run on this first sample had a remarkably similar response to those we had run on bulk Ge on GaAs samples, showing the Ge direct emission peak at around 0.8 eV and the indirect larger-band L-valley emission tailing off from 0.73 eV down 200 meV as seen in Figure 3.6, confirmed by taking a Varshni fit at low temperature (77 K) of pure Ge for the indirect bandgap energy. The fox ears around 1 eV could represent a measurement artifact and are present in each sample. No other distinguishing PL signature other than that of that of grown bulk Ge was detected for the first MQW sample.

CHAPTER 4: TOWARD BETTER-QUALITY MATERIAL

4.1 Changes and Improvements

Since the growth of the chamber's first MQW sample at Texas State, we made upgrades to both the MBE machine and the growth process. One major result of these upgrades is the first ever PL signature of a dilute germanium carbide MQW structure, and the first PL emission at wavelengths consistent with theory.

4.1.1 System Improvement and Additions

1. Oxygen has been reduced in the chamber by an order of magnitude, confirmed by RGA scans when compared to those from the earliest MQW growth. This is due to the amount of time the chamber has been in use in actively growing, the cleaner, nitrogen-purged openings for fixtures it has undergone under our supervision, and the addition of foil-wrapped heater-tape covering all gas plumbing into the chamber. XPS measurements detect no oxygen in our current growths, but these need to be validated by SIMS.
2. I added a while loop to the carbon precursor gas preparation step in the growth. Now a pressure condition must be met in one of the two gas cabinet Baratrons before the final pneumatic valve to the chamber opens. There is still a five-second pause to allow for gas build up before the final shutter is opened, and repeated testing shows reliable and consistent control of gas flow according to the flux measured on the BFM. The time necessary to get to a stable CBr_4 flux has been reduced by ten minutes. Furthermore (and much more importantly), it is now possible to maintain a stable CBr_4 flux for the duration of any growth because of this change.

3. A 25 °C decrease in both heater station (HTS) treatment and desorption of the wafer has now been implemented when growing on GaAs substrates, to help reduce decomposition of the GaAs.
4. We have implemented a new technique for calibrating our CAR heating system using the melting of indium droplets. Tuhin Dey has also gotten our BandiT pyrometer and band-edge thermometer working with the same goal in mind.
5. We added trisilane as a Si gas precursor to our gas cabinet to enable future growths of SiGeSn optical cladding layers for lasers.

4.1.2 MQW Changes and Improvement

1. Because temperature is king in epitaxial growth, the heating and cooling time periods between QW and barrier epitaxy is now controlled by a waiting function in the Molly software. A while loop, awaiting a temperature condition to be met (and failing if such an event takes too long), as well as a three-minute pause step in the code, have been inserted where once there was simply a hard timer. This helps to achieve reliable surface temperature control to reduce migration and decomposition of C and Sn.
2. One of my most recent samples included a 2 nm layer of cold germanium atop each quantum well layer to bury C and Sn and prevent decomposition. Further study is needed to validate this growth method, as the statistical growth of cold Ge may dominate during this period. However, the layer starts growing during the wafer heating phase which may offset this effect.
3. A 25 °C decrease in both heater station (HTS) treatment and desorption of the

wafer has now been implemented when growing on GaAs substrates.

4. Thinner Ge barrier layers of 5 nm, allowing for more light to penetrate during PL measurements, are now a staple of the current growth process, compared to the thicker ~20 nm layers from the previous growth. Our group's device modeling shows 5 nm barriers should be sufficient to keep the QWs independent of each other.
5. I helped implement a feedforward correction to minimize shutter transients. Shutter transients occur in MBE because each cell's temperature drops whenever its shutter opens, leading to a corresponding drop in flux. These transients particularly affect QW uniformity, since the fluxes drop over the course of roughly 1-2 minutes, and a QW might take only 3 minutes to grow. By proactively boosting the cell's heater power when the shutter opens, transients can be reduced. This project was first implemented using a circuit designed by Dr. Wistey and it was implemented and first demonstrated by Robert Hill, with subsequent improvements by Ahmed Ogunjobi, both under my supervision. Preliminary results have been promising, and the work is expected to be submitted for publication by early 2023.

4.1.3 Material Characterization Improvement

1. Two projects were successfully tackled by student teams from PHYS 5324 / MSEC 7310 using our GeSnC material: 1) making low resistance ohmic contacts to the surface of the epi, and 2) wet- and dry-etching of the epi to fabricate vertical sidewalls for laser waveguides. Publication of these works is pending.

2. We have learned and/or developed new characterization techniques and tools. Tuhin Dey now runs the XPS machine and with a deep level of understanding of the data, giving us a more direct measure of C and Sn content. This is critical because XRD alone of a ternary alloy, with two unknown material percentages, cannot reveal firmly these constituent amounts. In addition, I have set up a white light absorption system to try to measure direct bandgap absorption spectra.
3. Rutherford backscattering spectroscopy (RBS) measurements have been made on a series of our measurements thanks to a new collaboration we have with Joshua Cooper and Dr. Rachel Goldman's group at the University of Michigan at Ann Arbor. These measurements help to confirm the XPS data taken by Tuhin and have provided a clearer picture for material composition.

4.2 Other Characterization Techniques

4.2.1 Atomic Force Microscopy

Atomic force microscopy is one of the few techniques that operates at atomic resolution; traditional microscopes are unable to distinguish features smaller than ~200 nm due to the diffraction limit. AFM can measure both lateral and height distances of a few Angstroms.

AFM operates by bringing an extremely sharp tip on a flexible cantilever into contact with the surface of the sample being measured. Using a laser diode and a split photodetector, the bending of the cantilever as it contacts the surface is recorded, and the cantilever is rastered across the surface to create a height map. AFM is often done in "tapping" mode, in which the cantilever is vibrated slightly off the surface, but close

enough that the surface interaction perturbs the natural oscillation frequency. The force of interaction is monitored by an electronic feedback loop which tries to keep the average deflection of the cantilever constant throughout the scanning process. Different AFM probe heads have different resonant frequencies, and fundamentally it is the change in frequency, as caused by repulsive or attractive sample interactions, that is used to probe and measure sample features.

1. Scan Head
2. Vacuum Sample Stage
3. Probe Holder Base
4. Objective & Camera
5. Vacuum toggle switch
6. Photodetector signal display



Figure 4.1: Bruker Dimension ICON AFM, Texas State University SRO (courtesy of TXST SRO).

The AFM used for this work was a Bruker dimension ICON, shown in Figure 4.1. The measurements were performed in soft tapping mode using a non-conductive HQ.NSC14/Al BS tip with a spring constant of 5 N/m. To get accurate results, the gain settings in the software must be set in a way such that the trace and retrace amplitude measurement lines overlap. The first amplitude setpoint before every scan was set to 20 nm, at which point I would decrease it to around 15 or 16 nm. Modifying the amplitude setpoint until a better scan picture is rendered is the first step to getting good information, at which point I increase the proportional and integral gain to achieve better resolution. Typically, the proportional gain value should be 10x that of the integral gain value.

The AFM scanning was predominantly used to measure the root mean square (RMS) roughness of the thin film, but I also scanned some of the growths provided by Tuhin to get an idea of how many Sn droplets we may have on the surface of a GeSn sample, and their relative sizes.

4.2.2 Absorption

How light interacts with matter could have been the subtitle of this thesis, thus it only fits to include absorption measurements. Every semiconductor has an absorption spectrum that can be analyzed by simply shining light through the sample and measuring what comes out. This method offers one way to determine the fundamental bandgap of a material. Furthermore, if a material is homogenous and crystalline, as photon energy increases, a sharp absorption regime will be reached, which can correspond either to the direct bandgap band edge or an indirect bandgap band edge.

Absorption measurements were done on samples at room temperature using a halogen broadband white light source which sends light through an optical beam chopper into small slit into a Horiba Jobin Yvon iHR320 Monochromator. The monochromator uses the second of its three diffraction gratings corresponding to low-IR wavelength ($\lambda = 800\text{-}2500$ nm, 2000 nm blaze) to split and cycle the wavelengths of incoming light from low-to-high wavelengths in steps of 1 nm. The output from the diffraction grating is sent through an exit slit, just after which the sample being measured is placed inside a ring (made by me as one of my first ever projects here under Dr. Wistey) attached to the spectrometer and held in place by foam to not damage the sample surface. A Hamamatsu InGaAs photovoltaic photodetector, cooled to liquid nitrogen temperatures to reduce thermal noise (especially considering the wavelengths we are operating at go to near 500

meV), which can measure photon wavelengths up to from 0.9-2.4 μm is placed just after the sample to measure photons transmitted through the sample output. The detector's range is 0.9-2.4 μm wavelength, and it must be cooled with liquid nitrogen to reduce thermal noise, since the detector's bandgap is just 500 meV. Both the detector and the optical beam chopper are coupled to a SRS830 lock-in amplifier which then demodulates the signal, which is then recorded using the Horiba software package SynerJY and output plotted as a function of wavelength.

Preliminary measurements were made on a lightly p-doped, 180- μm -thick Ge sample, from which the indirect and direct bandgap room temperature energies were determined to be 0.64 eV and 0.79 eV, respectively, matching well established values for Ge. Modified Tauc plots were derived based on the equation

$$I(\hbar\omega) = I_0(\hbar\omega)e^{-\alpha d}$$

where I_0 as a function of photon frequency ω is the system response function (i.e. no sample is placed between the monochromator and the photodetector), I is the sample response as measured by the photodetector, and d is the sample thickness. The equation is rearranged to find the absorption coefficient α as

$$\alpha = \frac{1}{d} \ln \left(\frac{I_0}{I} \right)$$

which is then either squared or square-rooted and plotted against the spectrum of photon energies to form the modified Tauc plots. The nature of the optical transition is found by plotting either α^2 or $\alpha^{\frac{1}{2}}$ for a direct or an indirect transition, respectively, vs photon energy and extrapolating the respective bandgap energy as the x-intercept of the straight line-of-best-fit. In other words, the equation

$$(\alpha\hbar\omega)^{\frac{1}{r}} = (E_g - \hbar\omega)$$

is extrapolated to zero so the right-hand side can be solved for E_g .

4.3 Growths and Discussion

4.3.1 GeSnC/Ge on Semi-insulating GaAs Substrate

Two GeSnC/Ge MQW samples were grown on GaAs under the improved growth conditions discussed in section 4.1. For comparison's sake, the CAR TC was kept at 390 °C for the barrier and buffer growth. Due to an oversight, the hydrogen cell's filament was cold, just 4.5 A, and its shutter was closed. It is not expected that this will impact the growth of high-quality germanium at this temperature, though it may influence the growth of the QW layers at much lower temperatures. Furthermore, the temperature of the QW layers was reduced to 180 °C on the CAR TC after further characterization of bulk GeSnC was completed by Tuhin Dey. These samples differed from each other in one critical way, however: carbon content. The first sample's wells were grown under a CBr₄ beam-equivalent pressure of 1×10^{-7} Torr and the second's were grown under a BEP of 8×10^{-8} Torr (Figure 4.2). This represents one of the two potential shifts in the direction of our group's growth campaign, growing with increased C content (between 1-1.5% C) vs. increased Sn content (4% Sn).

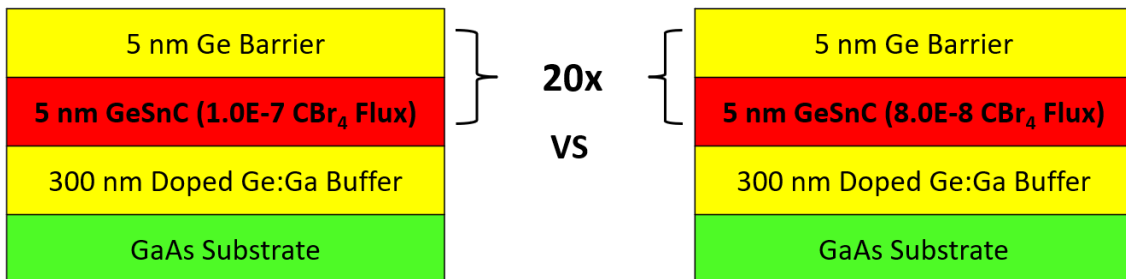


Figure 4.2: Two newest MQW growths on semi-insulating GaAs after improved growth techniques.

AFM measurements were taken on the sample with a CBr_4 flux of 1×10^{-7} Torr, the features of which have a maximum height differential of 5.9 nm. The surface, which had been prepared under the new 350 °C temperature regime and then desorbed under atomic hydrogen for fifteen minutes, was significantly flatter in AFM (see Figure 4.3), with no observable gallium or arsenic separation apparent from the measurements.

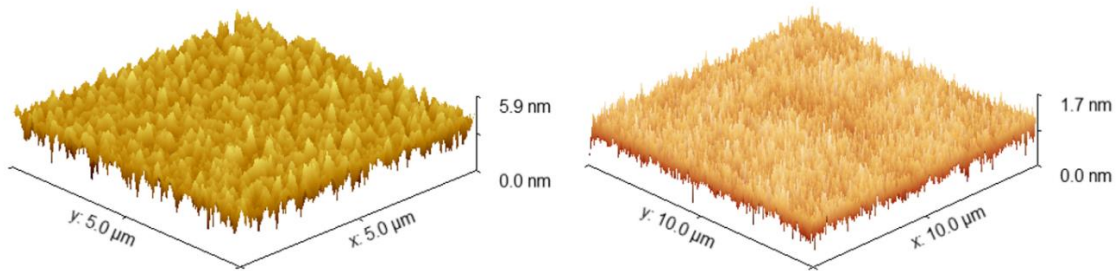


Figure 4.3: AFM measurement of GeSnC MQW on semi-insulating GaAs after process upgrades (left), AFM measurement of atomic-hydrogen-treated GaAs growth surface after 2-hour 350 °C bake showing no segregation.

While the sample was not as flat as we would wish, a 5.9 nm peak roughness is still relatively flat, and XRD peaks showed a few Pendellösung fringes, indicating better crystal quality than was previously shown for the similar sample shown in the third chapter.

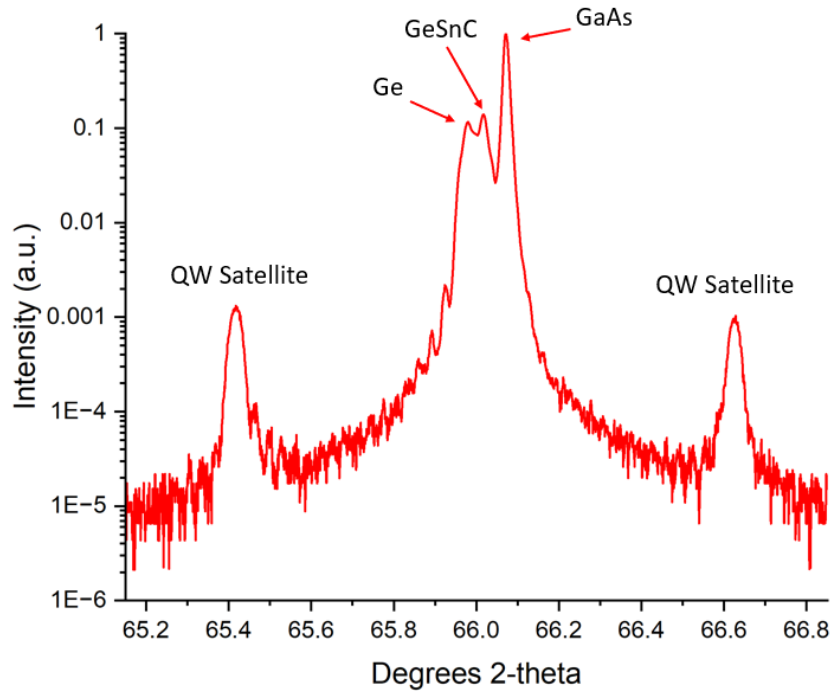


Figure 4.4: XRD measurement of GeSnC MQW on semi-insulating GaAs after improvements in growth technique.

The increase in angular separation of QW satellite peaks (see Figure 4.4) corresponds to the reduction of barrier size as compared to that of the previously shown MQW growth. Peak fitting with GlobalFit converges for a barrier thickness of 5.5 nm, which is very close to the design thickness of 5.0 nm.

4.3.2 GeSnC/Ge on P-Type Ge Substrate

Consistent with Tuhin Dey's work in optimizing bulk $\text{Ge}_{1-x-y}\text{Sn}_x\text{C}_y$ on Ge substrates, two samples like those reported above were grown on low-doping concentration p-type Ge. However, instead of 20 QW layers, only five were grown on each of the two samples, intentionally terminated by an active GeSnC QW layer to investigate by AFM. RHEED imaging taken just after the growth of the first QW layer (see Figure 4.5) of one of the samples reveals streaky 2x patterns, indicating good epi surface morphology.

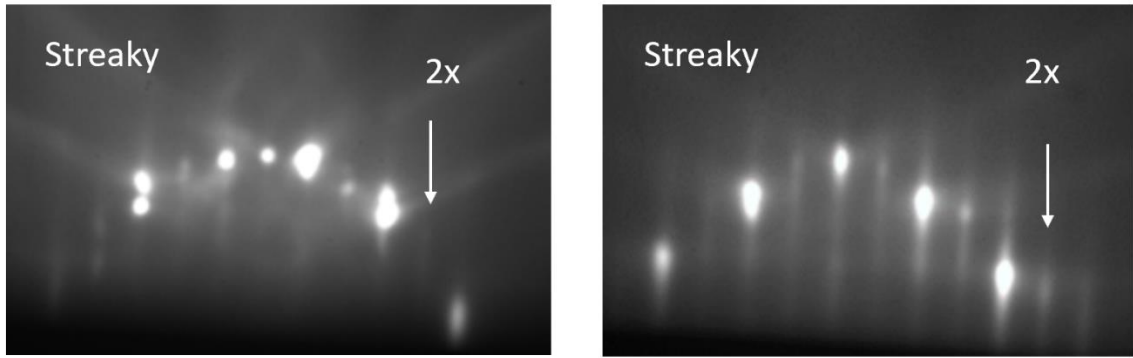


Figure 4.5: (left) RHEED surface reconstruction of first QW layer of GeSnC on p-Ge, (right) p-Ge growth surface after atomic-H and 700 °C desorption treatment.

However, AFM imaging revealed an unexpectedly poor surface quality. Previous bulk growths using the same fluxes and temperatures did not have such negative results. Note, again, the depth of the quantum wells to be 5 nm, whereas the difference in peak-to-valley depth on the surface of the epi was measured as large as 40 nm. Each of the five wells and barriers were 5 ± 1 nm thick, and the deepest of the holes interrogated by AFM is 40 nm below the growth surface. This indicates the bottom of the epi is actually very near the surface of the buffer layer. This honeycomb-shaped growth, which is consistent through the two samples grown at slightly different temperatures, shows that I did not grow a quantum well at all, but an amalgam of randomly patterned quantum dots (Figure 4.6).

The growth of the colder of the two samples had a CAR TC setpoint of 160 °C, and the growth recipe for that growth was still simply based on timing. Looking back through the growth data later, I noticed that the setpoint of 160 °C was never reached during this growth, which means that the CAR heating elements never switched on while the QW layer was being grown. This may turn out to be key, as Tuhin Dey has demonstrated that the CAR heating elements heat the surface of the wafer far past its

setpoint for a small amount of time.

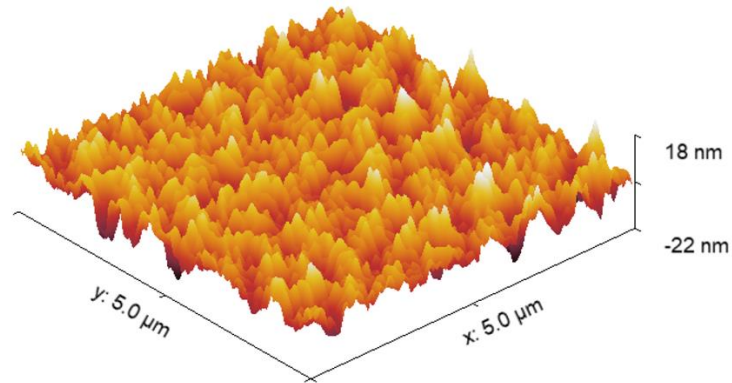


Figure 4.6: AFM measurement of GeSnC MQW structure on p-Ge sample grown at 160 °C.

Although the AFM showed a rough surface as seen in Figure 4.6, I sent these samples to UT Austin to have PL measurements performed on them. As Dr. Wistey reminds his group members: a negative result is still a result if we learn from it.

Without further ado, we had PL!

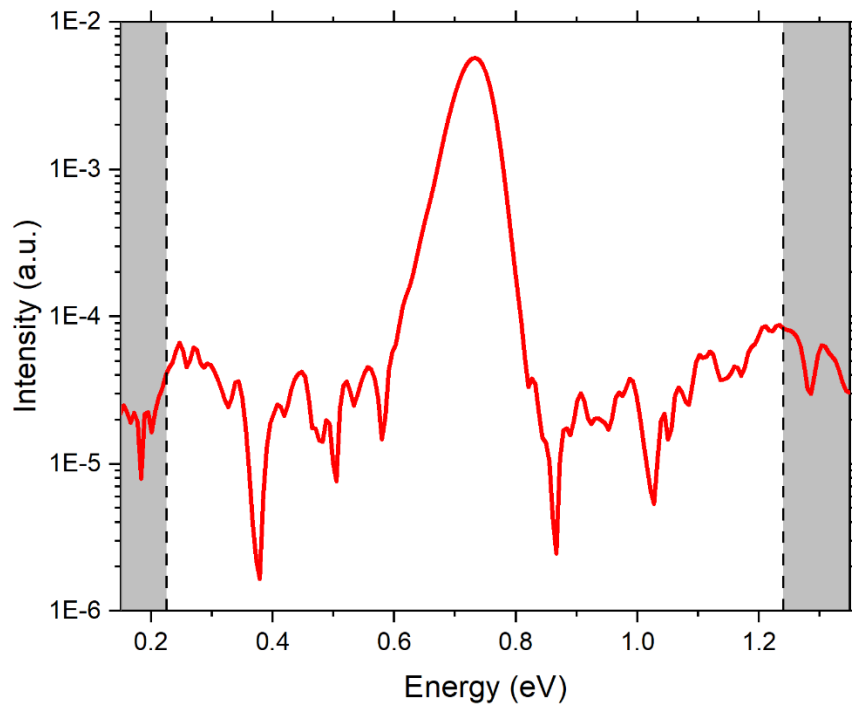


Figure 4.7: PL measurement of GeSnC MQW structure on p-Ge sample grown at 160 °C.

None of the other samples, save one of Tuhin Dey’s bulk GeSn samples, emitted with as much intensity, and none had such a pronounced singular peak (Figure 4.7). Comparing this data to other PL data we received from Dr. Muhowski, each of which contained the identifiable “rabbit ears” pertaining to the direct and indirect bandgap emission energy, this peak emits more strongly by a factor of six and at an energy 70 meV lower than that of the direct emission peak (see Figure 4.8).

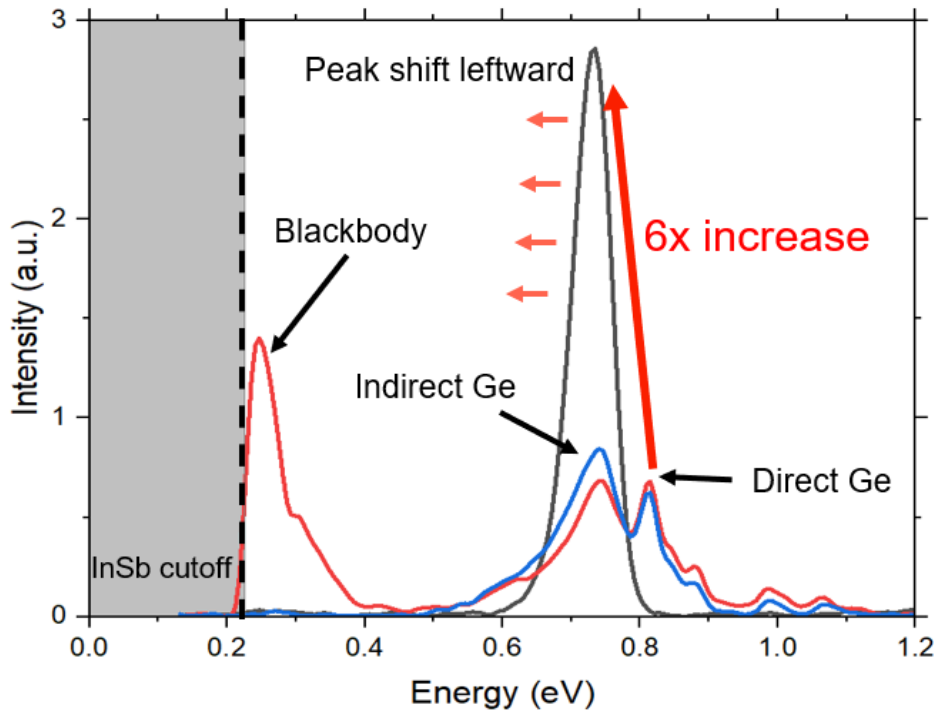


Figure 4.8: PL measurements of three different MQW samples on a linear scale. The red and blue curves demonstrate typical PL signatures from all other MQW samples. The black curve is the same as in Figure 4.7.

This demonstrates a significant achievement in the dilute carbides, and it is a sign that our research is progressing in the right direction.

4.3.3 Direct Absorption of Bulk GeSnC

The absorption process and understanding implemented for finding the direct bandgap energy for a 180 μm thick low-doping concentration p-Ge wafer was applied to

data taken from measurements on a bulk GeSnC sample grown on a 180 nm buffer of Ge atop a GaAs substrate. The epi layer was 1 μm thick, which is too thin to reliably find the indirect bandgap energy level associated with the material, and the direct transmission seemed to dominate. A linear fit was applied to the area of the curve where the difference between the system response and the epi response increases exponentially. The assumption was made that the system response for the purposes of calculation would be represented by the absorption of a piece of equally thick epitaxially grown Ge atop a GaAs substrate, with the epi response being the GeSnC bulk on GaAs.

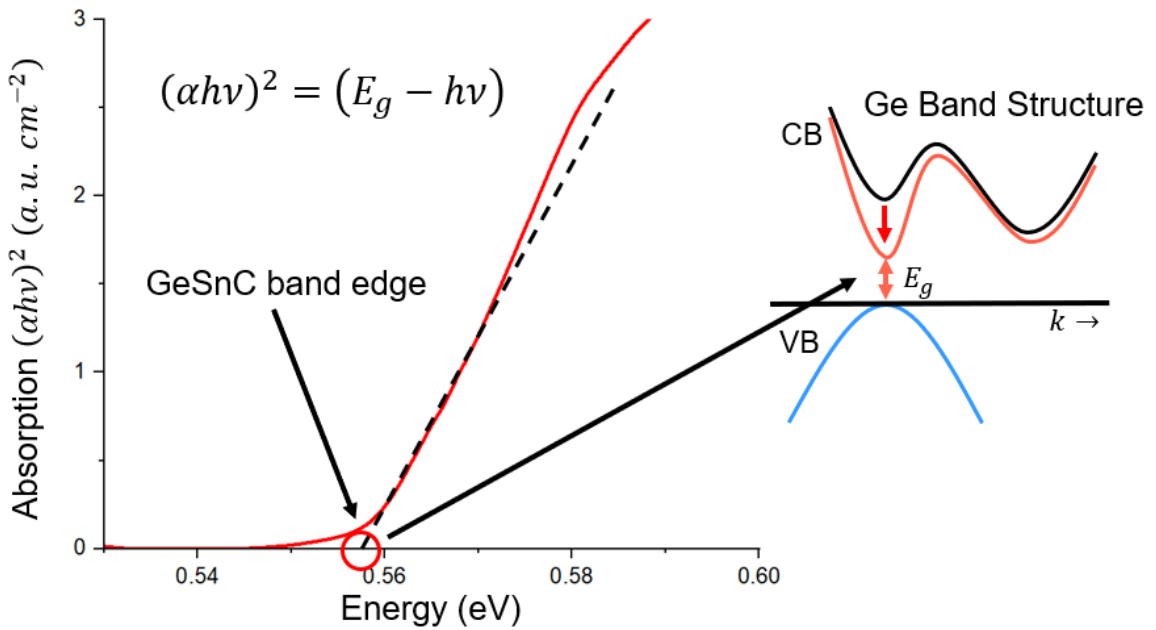


Figure 4.9: Direct bandgap absorption plot of bulk GeSnC.

As is evident when comparing the direct bandgap emission of this sample to the PL emission results from the MQW sample in Figure 4.7, the difference in energies is surprising. I attribute this primarily to the fact that the composition of both materials can only be estimated by bulk growths under similar conditions, and that to date no such measurements have been done on a bulk GeSnC growth in which the CAR heater was off

for the duration of the growth and the temperature held relatively constant around 170 °C. As expected, temperature plays the most vital role in all the epitaxial growth conducted by me and the rest of the team.

However, the fact that there is such a significant shift downward in energy as seen in Figure 4.9 from the same absorption method applied to low-doping concentration bulk p-Ge is further validation that I grew a direct bandgap material, especially considering this band edge to be at a lesser energy than the indirect bandgap of Ge (as proven both in literature and by my measurements). Still, further study and data development is needed to be conclusive.

CHAPTER 5: CONCLUSION AND FUTURE WORK

5.1 Conclusion and Impact

The growth of dilute carbide MQW heterostructures presented in this work marks a significant milestone toward the successful integration of monolithically grown direct bandgap Group-IV semiconductors on silicon for lasers, amplifiers, modulators, and other Si CMOS compatible devices. Of utmost importance lies both in the first experimental demonstration of PL matching theory (and second in history) [25] and direct bandgap proof from absorption of GeSnC. The novel approaches discussed in the bulk GeC, GeSn, and GeSnC development by me, Tuhin Dey, and Dr. Shamim Reza, working under Dr. Mark Wistey, led directly to its implementation as the active layer in a MQW heterostructure, and the research only begins here.

Gas source CBr₄, although seemingly not the optimal precursor for substitutional carbon compared to 4GeMe, has proven to have remarkable utility in seeking direct bandgap Group-IVs. Working in tandem with Sn, and indeed with the demonstrable aid these atoms give each other during the growth process, a growth regiment for creating substitutional C and Sn in a Ge lattice has been shown to be successful and the science of this material can have far-reaching effects. State-of-the-art industrial fabrication facilities currently implement costly – both in time and safety – practices such as the use of arsenic in direct bandgap device production and the chip-bonding method used to glue devices to the silicon substrate. This work demonstrates the potential for a new class of material with the benefit of doing away with these practices, in addition to propping up new research programs to further the science.

HR-XRD revealed the existence of the active QW layers, and while AFM is left

wanting in how flat the material was shown to be, this still gave rise to PL emission, proving computational theory for the material. Substitutional C and Sn as shown by Tuhin Dey and Dr. Shamim Reza, and grown in large part by me, laid the foundation for this achievement.

5.2 Summary

My contribution toward the group's goal can be distilled into two parts:

1. Firstly, I have an appreciable understanding of the workings of all aspects of an MBE system. Using mechanical, electrical, plumbing, vacuum science, and computational knowledge I've gained over the course of the past five years (indeed, from the ground up. I was the one that initially plugged the machines into the 3-phase power and first heard them turn on!), I helped in all phases of the growth, characterization, and research of bulk materials that have led to numerous research publications and conference talks, one of which was given by me. The contribution here was that of the laboratory technician and an MBE grower. I built the hydrogen purifier system from scratch, which is itself a pivotal part of our growth process. I built a CAR puller which renders the job of machine maintenance on the heaviest and most costly part of the MBE doable inside a glove bag (see Appendix). One of my very first projects was the simple machining of a little disk that is now used by me for absorption measurements. Each of these many projects over the years have allowed for this point to be reached in our research.
2. The development of a Group-IV bulk material to be used as the active layer in MQW devices was the project I had set out to complete at the beginning of my

master's degree. Three important tools used to characterize this new material were learned/developed with this goal in mind: AFM reveals relatively flat surfaces in most of the QW samples I grew, save the two from the most interesting series I grew that gave us PL. A 40 nm depth disparity over a MQW heterostructure may provide key insight into the eventual development of the kinds of devices discussed; XRD showed distinguishable QW satellite peaks, a feature that would otherwise not be in the data without the presence of these layers; Absorption revealed for the first time that our bulk material shows the distinct signature of having a direct bandgap, especially considering the energy value to be more than 10% lower than the indirect bandgap energy of intrinsic Ge. All this goes hand in hand with my capacity as an MBE grower and technician. The contribution here was that of a research scientist.

5.3 Future Work

5.3.1 Optimizing GeSnC MQW Heterostructures

1. The effects of hydrogen passivation of the surface of each QW layer can be studied, as well as the effects of annealing, though the temperature should not be increased too much at risk of the Sn and C segregating even under the top-most layers.
2. The variation of C and Sn content in the active layers, as determined by continuing study of bulk GeSnC, can potentially lead to even larger incorporation of substitutional C. This dilute carbide needs further investigation, as this may very well only scratch the surface of how much C it is possible to incorporate.
3. The shutter transients project completion for extremely fine control of QW layer

thickness is paramount for device optimization.

4. Investigating the effects of growing GeSnC MQW heterostructures under ambient atomic hydrogen should be undertaken. Tuhin Dey's work has demonstrated that the presence of H_1 helps to incorporate both C and Sn in bulk material.

5.3.2 Device Fabrication

The two projects assigned to the students in PHYS 5324 / MSEC 7310 have resulted in promising results (vertical sidewall etching) and one pending publication (ohmic contacts). Since I know that PL is now possible with GeSnC grown on lightly-doped p-Ge, the next step is to make this process reliable and then try and build a device out of it. With these results, I'd seek to make a simple LED first as a proof of principle. However, a working room temperature laser is still the goal.

APPENDIX 1: TAKING FLUXES

The CAR has a few attachments that are worth noting.

1. Rotation of the wafer, as powered by the stepper motor attached to the device, is desired for growth uniformity. While there are other useful growth mechanisms we can investigate without using the CAR's rotation, I have yet to not use this capability aside from when we wish to simply outgas any cells to clean them (essentially, we heat the filaments on the desired cell to ~ 20 °C hotter than any growth temperature we would ever take it to, then open the cell's shutter to deposit material to help rid the sources of any impurities that may have found themselves inside the crucible). This process is done on either a "throw-away" wafer, or on the side of the CAR itself, a process that helps to bury any unwanted particles that have both collected on the sidewalls of the chamber and on the CAR itself.
2. Two sets of heating coils wrap around the inner and outer portions of the CAR, which help maintain consistent temperature. We monitor this temperature via thermocouple, and recently through use of our BandIT camera and software, with the camera pointed directly at the surface of the wafer (or, more generally, the center of the CAR) looking through a dedicated viewport, connected to our second-of-eight shutters (insert type of glass here). This software can take in both blackbody and band-edge information, allowing us to read more accurately the temperature of our growth surface.
3. The backside of the CAR, opposite to where we load wafers, is outfitted with one of the two ion gauges found in the main MBE chamber, the other one being

located behind a large shutter and used for more general pressure monitoring. The ion gauge attached to the CAR, named the Beam Flux Monitor (BFM), is the primary tool we use to take fluxes before each growth we do. There are times during which flux-taking is unnecessary for growths, such as dump growths (cleaning the source material, as mentioned above), and for consecutive growths using the same materials used in the previous growth. It is imperative, in this second case, to keep the cell(s) at the same prescribed temperature that the initial flux measurements ask for.

Outlined below are the steps for taking fluxes in our chamber:

1. Upon arriving in the lab in preparation for a growth, I set each cell's Eurotherm temperature to around its expected growth temperature (as noted from the most recent growth used with this cell). This will cause the power delivered from the Sorenson power source dedicated to this cell to begin ramping up until the desired growth temperature is met. I then leave the cell at its growth temperature for twenty to thirty minutes to stabilize the now-liquid- (or, "mostly solid", in the case of our gallium cell used mainly for doping-concentration epitaxy) phase solid source material. A typical value for the set growth temperature for the tin cell 990 °C, and the germanium can range from 1240 °C to 1270 °C. These values can be relatively rough estimates, as our method involves taking fluxes at five different temperatures, around the initial growth temperature, and fitting these values on an Arrhenius curve. I go into detail about this next, showing what taking fluxes is like when I wish to use both our tin and germanium solid sources.
2. Once the cells have been heated to their respective temperatures and left there to

stabilize, I then start the flux-taking code in Molly. The code will then be stepped through as follows:

- a) User makes sure to power the BFM and turn it towards the cells (parallel to the ground, which is the orientation pointed towards the center of the cell matrix in this chamber's case). User makes sure the cells are powered, and that the machine is otherwise ready to take fluxes (water is flowing, no noticeable electrical fluctuations in Sorenson power, etc).
- b) The germanium cell is set to 10 °C colder than its prescribed temperature, and the tin cell to 20 °C colder.
- c) Check set temperatures to verify whether the cells are ready to take fluxes. If the cells haven't reached the setpoint yet, wait until they do and pause for the stabilization period.
- d) Once these conditions have been met, the BFM will take readings for three minutes of "background" pressure. Accounting for this pressure is necessary for real flux values. Twenty of these values are stored, two of which have been thrown away as "outliers", since our BFM sometimes reads faulty values (-999 Torr and +8996 Torr!). The remaining eighteen values are averaged, and this value is stored as "background 1".
- e) Once the background flux is taken, the germanium cell shutter is then opened for its flux to be read by the BFM. The shutter remains open for three minutes, over which the first minute no data is recorded to account for shutter transients (project noted in the *Future Work* section). The second- and third-minutes' data are then taken, averaged in much the same

way as the background fluxes, and this value is then stored as the shutter-open flux.

- f) The Ge shutter is now closed, and another three-minute pause is initiated, during which the Ge cell is heated by 5 °C. Over the first minute, no data is taken to allow for stabilization of the BFM, having recently been coated by Ge and with some Ge floating around the chamber. The second- and third-minutes' data are then taken, averaged again after throwing away two more outliers, and this value is then stored as “background 2”.
- g) The tin flux-taking is nearly the same as the germanium's, the only difference being the Sn is heated in 10 °C steps.
- h) The “real” flux for both cells is then calculated by averaging the two background measurements for each and subtracting this averaged background value from the open-shutter value corresponding to its particular cell. This is what we deem the flux for that particular temperature for this flux-taking run.
- i) Repeat steps *d through f* four times, for a total of five values. For instance, if I set my setpoint for the germanium cell to 1255 °C and the tin cell to 990 °C, I then have five real values for the germanium flux which range from 1245-1265 °C in steps of 5 °C, and for the tin flux which range from 970-1010 °C in steps of 10 °C. The reason for the different step values is that the tin concentration we have desired up until this point has been low relative to tin's melting point, for instance a tin cell temperature of 970 °C corresponds to around a 4×10^{-9} Torr. This value is (typically, depending

on how clean the chamber is and when it was last used) under the noise floor of the BFM, and more accurate measurements would generally be taken at higher temperatures. We balance wasting too much source material and getting reliable fluxes with this method.

APPENDIX 2: SAMPLE PREPARATION

A typical sample preparation, start-to-finish, goes through a process as follows:

1. After being cleaved into the desired size and shape depending on the uniblock (wafer holder) used, each sample is loaded onto the load-lock trolley, which is fed through an o-ring sealing door into the load-lock.
2. The door is closed, at which point we begin the vacuum process: first by using a scroll pump to bring the environment to the E-02 Torr regime, then by a turbo pump (backed by this same scroll) to reach the E-08s.
3. An eight- to ten-hour bake at 200 °C is performed on this isolated section of the chamber to separate any water and other unwanted particles from both the growth surfaces and the vacuum environment, which lowers the pressure by a factor of ten.
4. After baking, we open the gate valve and roll the trolley into the buffer chamber. We then bake an awaiting growth wafer on our heater station (HTS). Both types of wafers receive their respective two-hour bake: GaAs at 350 °C and Ge at 400 °C. This process cleans the surface by removing any lingering surface hydrocarbons, as well as any water that managed to make it to the surface.
5. Our wafer is then transferred into the growth loading section of the buffer chamber, grabbed by an extending arm, and placed inside the chamber on the CAR (Continuous Azimuthal Rotation), the reverse side of which has a Beam Flux Monitor (BFM) attached. Once the wafer is loaded, we are ready for the final oxide desorption step.
6. We begin to heat both the hydrogen cell's filament to 2250 °C (standard operation

at 8.5 A and ~22.9 V) and the CAR's inner and outer filaments to the desired desorption temperature (350 °C for GaAs and 400 °C for Ge). It is instructive to monitor the Residual Gas Analyzer (RGA) during this process, as we can watch what the heating of each individual element in our chamber does to especially the water and hydrocarbon levels. Once both sets of filaments are at temperature, we begin rotation of the CAR at 10 RPM and open the shutter to the hydrogen cell. Fed in through the gas plumbing lines is diatomic hydrogen, which splits into atomic hydrogen at a 1-to-10 splitting ratio. The H₁ acts as a getter for any surface oxides or hydrocarbons present on the sample. To desorb the oxide layers it takes around fifteen to twenty minutes for a GaAs sample, and the Ge sample takes an extra step where it is brought to 650 °C for fifteen minutes. *In situ* Reflective High-Energy Electron Diffraction (RHEED), for which I go into further detail later, is used to monitor the quality of the growth surface during desorption.

7. Upon satisfactory RHEED patterns being observed, we bring the CAR to the desired growth temperature and cool the hydrogen filament back to 10% power (unless Atomic H is used in the growth, in which case we leave the cell at power). We are now ready to grow.

APPENDIX 3: EQUIPMENT MAINTENANCE

Early and Current Chamber Oxygen Content

Every time a new wafer is introduced to the chamber, it comes with some intrinsic oxide layer that must be desorbed (as outlined in *Appendix II*). The amount of oxygen on a wafer's surface, however, is estimated to be only ~ 25 Å, consisting of As_2O_3 , Ga_2O_3 , GaAsO_3 , and GaAsO_4 , and the most volatile form of Ga_2O , in some parts. This atomic thickness has not shown up recently in RGA scans of the chamber during oxide desorption, that is, the O_2 levels do not peak above the noise floor of the device. However, water has been an ever-present issue in our chamber. This is particularly due us not baking our chamber, as many other MBE groups do, because we recently cracked welds in both chambers after having done so. When water contacts the heated growth surface, there is the opportunity for the hydrogen to get removed from the molecule and for the oxygen to stay behind as a defect. ToF-SIMS confirms oxygen content in throughout early growths in this chamber.

The overwhelming majority of oxygen doesn't come from the desorption process, however. It comes from background oxygen already present in the chamber (even after months and months of growths!), any glove-bag openings we may perform and aren't perfect in not exposing our chamber to oxygen, and to the occasional turbo pump spin-down sequence that invariably will introduce some foreign contaminants. Vacuum is a fickle mistress. Levels have decreased by an order of magnitude since December 2021 (over the course of a year), and it's (in part) to this that I attribute our ability to grow PL-worthy direct bandgap samples.

Building of the Hydrogen Purifier

To briefly go into probably my most important machine modification, I planned and built the plumbing to and from a palladium-mesh hydrogen gas filter meant to get our 4N (that's 0.9999%, or "four 9's" pure). I did not built the filter itself; we bought that piece online. However, the planning, welding, fitting, and everything in between was completed by me. I'd like to thank Dr. Piner for letting me use his orbital welder. Now we have uber-clean hydrogen fed into our chamber!

APPENDIX 4: GOAT BLOOD FEES

Silicon photonics can reduce an entire table's worth of optics down to one chip, so we figured we'd start a project with just this in mind: Goat Blood Fluorescence Excitation Emission Spectroscopy (FEES). Anemia kills more livestock than the next four cause of death combined. Here we sought the proof of principle for a device that could detect anemia in any goat far more efficiently than the current detection method, and indeed try to save it in the process. In the long term, this may prove useful for human disease detection as well. This was another of my projects I undertook, predominately during my MS.

Two undergrads (Robert Hill and Nolan Groves) and I teamed up to measure the output of and parse the data from samples of known healthy vs anemic goat's blood harvested from live goats at the Fulton Ranch outside of San Marcos. Much like the absorption measurements done on our thin films, I used our Horiba Jobin Yvon iHR320 spectrometer – although this time I modified an existing Horiba LabVIEW program to fit my needs – and its wavelength-cycling capacity in steps of 1 nm across the entire visible spectrum to shine each wavelength on any given sample and read the response. One important distinction that had to be made between our lab and all others in the building was that it had to be inspected and passed as a BSL-2 safety lab, so I wrote the SOP for our measurement and cleanup processes and made sure the lab setup justified the certification.

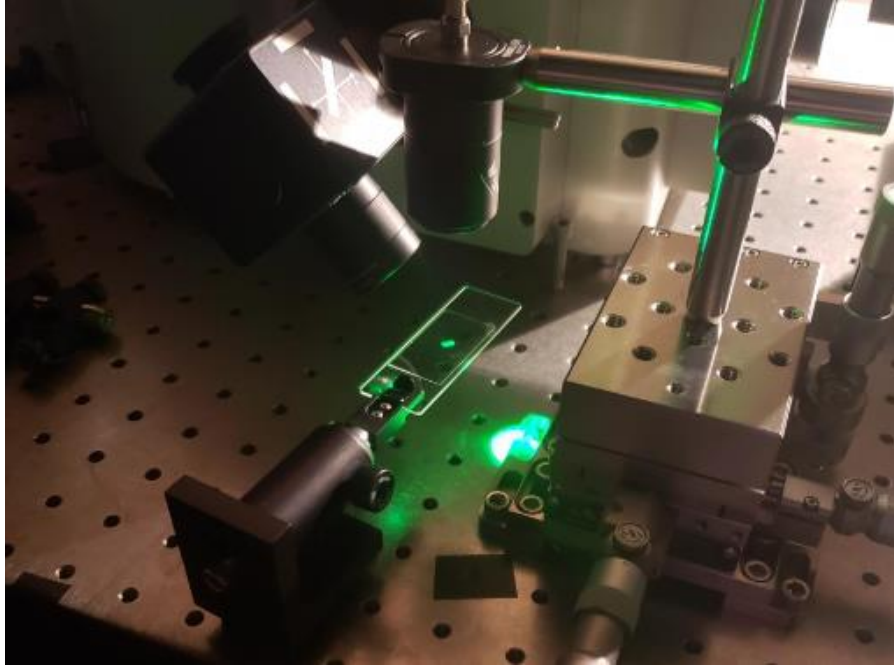


Figure A1.1: Microscope slide with slide cover over anemic goat blood sample.

Unfortunately, no noticeable signature was detectable between healthy vs anemic samples, save that the anemic samples were less red. We were looking for any “off-axis” data, i.e., when a light of a particular wavelength is shone on the sample, does a different wavelength signature emit or is the emission simply the wavelength of the light source? Though, there’s always something to learn from failure, and that we got a program running that could tell the relative difference between the brightness of the two types of sample responses was promising. It should be noted that even using a more powerful light source would likely result in no more fruitful data, as even at this beam power the blood would dry out quickly. More study is needed to validate this method.

Finally, I took several blood samples from goats myself, which seems very much outside the scope of a physics degree.

REFERENCES

- [1] “What is the significance of Moore’s Law? | EEFAQ,” *CircuitBread*.
<https://www.circuitbread.com/ee-faq/what-is-the-significance-of-moores-law-and-is-it-still-true-today>.
- [2] R. E. Camacho-Aguilera, Y Cai, N. Patel, J T. Bessette, M Romagnoli, L. C. Kimerling, and J. Michel, “An electrically pumped germanium laser,” *Optics Express*, vol. 20, issue 10, pp. 11316-11320, 2012.
- [3] G. He and H. A. Atwater, “Interband Transitions in $\text{Sn}_x\text{Ge}_{1-x}$ Alloys,” *Phys. Rev. Lett.*, vol. 79, issue 10, pp 1937-1940, 1997, doi: 10.1103/PhysRevLett.79.1937.
- [4] J. Menendez, P.M Wallace, C. Xu, C. L. Senaratne, J. D. Gallagher, and J. Kouvetakis, “Materials Physics of GeSn-based Semiconductor Lasers,” *Materials Today: Proceedings*, vol. 14, part 1, pp. 38-42, 2019, doi: 10.1016/j.matpr.2019.05.048.
- [5] M. S. Reza, “Direct Bandgap Germanium for Active Silicon Photonics Applications,” Ph.D. dissertation, Dept. Materials Science, Engineering, and Commercialization, Texas State Univ., San Marcos, TX, 2022.
- [6] L. C. Kimerling, J. Michel, and J. Liu, “Monolithic Ge-on-Si lasers for large-scale electronic-photonic integration,” *Semicond. Sci. Technol.*, vol. 27, 2012, doi: 10.1088/0268-1242/27/9/094006.
- [7] Y. Zhou et al., “Electrically injected GeSn lasers on Si operating up to 100 K,” *Optica*, vol. 7, issue 8, pp. 924-928, 2020, doi: 10.1364/OPTICA.395687.
- [8] M. Qi, W. A. O’Brien, C.A. Stephenson, N. Cao, B. J. Thibeault, and M. A. Wistey, “Stability of Tensile-Strained Ge Studied by Transmission Electron Microscopy,” *International Silicon-Germanium Technology and Device Meeting (ISTDM)*, pp. 1-2, 2012, doi: 10.1109/ISTDM.2012.6222505.
- [9] “Band structure and carrier concentration of Germanium (Ge),” www.ioffe.ru.
<https://www.ioffe.ru/SVA/NSM/Semicond/Ge/bandstr.html> (accessed Oct 20, 2022).
- [10] “Band structure and carrier concentration of Gallium Arsenide (GaAs),” www.ioffe.ru.
<https://www.ioffe.ru/SVA/NSM/Semicond/GaAs/bandstr.html> (accessed Oct 20, 2022).
- [11] C. A. Stephenson et al., “Band structure of germanium carbides for direct bandgap silicon photonics,” *J. Appl. Phys.*, vol. 120, no.5, 2016, doi: 10.1063/1.4959255.
- [12] C. A. Stephenson, M. Gillett-Kunnath, W. A. O’Brien, R. Kudrawiec, and M. A. Wistey, “Gas Source Techniques for Molecular Beam Epitaxy of Highly Mismatched Ge Alloys,” *Crystals*, vol. 6, no. 12, p. 159, 2016, doi: 10.3390/cryst6120159.

- [13] Kolodzey et al., “Temperature varying photoconductivity of GeSn alloys grown by chemical vapor deposition with Sn concentrations from 4% to 11%,” *Journal of Applied Physics*, vol. 119, issue 9, 2016, doi: 10.1063/1.4942851.
- [14] “Quantum well,” *Wikipedia*. https://en.wikipedia.org/wiki/Quantum_well (accessed Oct. 19, 2022).
- [15] Bowers et al., “Reliability of InAs/GaAs Quantum Dot Lasers Epitaxially Grown on Silicon,” *IEEE Journal of Selected Topics in Quantum Electronics*, vol. 21, issue 6, pp. 1900708, doi: 10.1109/JSTQE.2015.2418226.
- [16] M. A. Wistey, Y.-Y. Fang, J. Tolle, A.V.G. Chizmeshya, and J. Kouvetakis, “Chemical routes to Ge/Si (10) structures for low temperature Si-based semiconductor applications,” *Appl. Phys. Lett.*, vol. 90, issue 8, 2007, doi: 10.1063/1.2437098.
- [17] “The Nobel Prize in Physics 2000,” *NobelPrize.org*. <https://www.nobelprize.org/prizes/physics/2000/kroemer/lecture/> (accessed Nov. 11, 2022).
- [18] “Density of States,” *Engineering LibreTexts*, Jul. 28, 2016. [https://eng.libretexts.org/Bookshelves/Materials_Science/Supplemental_Modules_\(Materials_Science\)/Electronic_Properties/Density_of_States](https://eng.libretexts.org/Bookshelves/Materials_Science/Supplemental_Modules_(Materials_Science)/Electronic_Properties/Density_of_States).
- [19] J. Singh, *Physics of Semiconductors and Their Heterostructures*. McGraw-Hill, 1993.
- [20] J.W. Matthews and A. E. Blakeslee, “Defect in epitaxial multilayers: I. Misfit dislocations *,” *Journal of Crystal Growth*, vol. 27, pp 118-125, 1974, doi: 10.1016/S0022-0248(74)80055-2.
- [21] Y. Ota, “Growth of high quality Ge MBE film,” *Journal of Crystal Growth*, vol. 61, issue 3, pp. 431-438, 1983, doi: 10.1016/0022-0248(83)90171-9.
- [22] Wikipedia Contributors, “Silicon-oxygen tetrahedron,” *Wikipedia*, Mar. 20, 2017. https://en.wikipedia.org/wiki/Silicon%E2%80%93oxygen_tetrahedron.
- [23] T. Dey, M. S. Reza, A. Arbogast, M. W. Holtz, R. Droopad, S. R. Bank, and M. A. Wistey, “Molecular beam epitaxy of highly crystalline GeSnC using CBr₄ at low temperatures,” *Appl. Phys. Lett.*, vol. 121, issue 12, 2022, doi: 10.1063/5.0102093.
- [24] “Bragg’s Law,” *Gsu.edu*, 2019. <http://hyperphysics.phy-astr.gsu.edu/hbase/quantum/bragg.html>.
- [25] I. A. Gulyas, C. A. Stephenson, Q. Meng, S. R. Bank, and M. A. Wistey, “The carbon state in dilute germanium carbides,” *Journal of Applied Physics*, vol. 129, issue 5, doi: 10.1063/1.5112057.